Title

K2PChannel C-Type Gating Involves Asymmetric Selectivity Filter Order-Disorder Transitions

Journal

Biophysical Journal, 120(3)

ISSN

0006-3495

Authors

Natale, Andrew M
Lolicato, Marco Gaetano Lorenz
Abderemane-Ali, Fayal
et al.

Publication Date

2021-02-01

DOI

10.1016/j.bpj.2020.11.898

Peer reviewed

STRUCTURAL BIOLOGY

K_{2P} channel C-type gating involves asymmetric selectivity filter order-disorder transitions

Marco Lolicato[1]*†, Andrew M. Natale[1]*, Fayal Abderemane-Ali[1], David Crottès[2], Sara Capponi[1‡], Ramona Duman[3], Armin Wagner[3], John M. Rosenberg[4], Michael Grabe[1,5§], Daniel L. Minor Jr.[1,6,7,8,9§]

K_{2P} potassium channels regulate cellular excitability using their selectivity filter (C-type) gate. C-type gating mechanisms, best characterized in homotetrameric potassium channels, remain controversial and are attributed to selectivity filter pinching, dilation, or subtle structural changes. The extent to which such mechanisms control C-type gating of innately heterodimeric K_{2P}s is unknown. Here, combining K_{2P}2.1 (TREK-1) x-ray crystallography in different potassium concentrations, potassium anomalous scattering, molecular dynamics, and electrophysiology, we uncover unprecedented, asymmetric, potassium-dependent conformational changes that underlie K_{2P} C-type gating. These asymmetric order-disorder transitions, enabled by the K_{2P} heterodimeric architecture, encompass pinching and dilation, disrupt the S1 and S2 ion binding sites, require the uniquely long K_{2P} SF2-M4 loop and conserved "M3 glutamate network," and are suppressed by the K_{2P} C-type gate activator ML335. These findings demonstrate that two distinct C-type gating mechanisms can operate in one channel and underscore the SF2-M4 loop as a target for K_{2P} channel modulator development.

INTRODUCTION

K_{2P} channels regulate nervous, cardiovascular, and immune system functions (*1*, *2*) through the action of their selectivity filter (C-type) gate (*3*–*6*). C-type gating occurs in many potassium channel classes and displays a hallmark sensitivity to external potassium due to its dependency on interactions between the permeant ions and selectivity filter (*4*, *6*, *7*–*12*). Although structural studies of exemplar homotetrameric potassium channels have uncovered various types of selectivity filter rearrangements attributed to C-type gating (*11*, *13*–*19*), there remains a debate about whether the essence of C-type gating involves pinching (*11*, *13*–*16*), dilation (*12*), or more subtle selectivity filter changes (*17*–*19*). Furthermore, although structural studies of different K_{2P} family members have revealed changes in the transmembrane helix conformations that affect activity (*20*–*26*), no selectivity filter conformational changes that could explain how K_{2P} C-type gating occurs have been observed. This lack of a structural framework has left open questions regarding the extent to which K_{2P} C-type gating mechanisms resemble homotetrameric channels (*11*, *13*–*18*) and whether the innate heterodimeric K_{2P} selectivity filter architecture confers unique properties to their C-type gates.

Here, combining x-ray crystallography of K_{2P}2.1 (TREK-1) in different potassium concentrations, potassium anomalous scattering, molecular dynamics, and functional studies, we uncover extraordinary, asymmetric, potassium-dependent structural changes that trigger K_{2P} C-type gating. We show that low potassium concentrations evoke conformational changes in selectivity filter strand 1 (SF1), selectivity filter strand 2 (SF2), and the SF2-transmembrane helix 4 loop (SF2-M4 loop) that destroy the S1 and S2 ion binding sites through a mixture of pinching of SF1 and dilation of SF2, leveraging the fundamentally heterodimeric nature of the K_{2P} selectivity filter to exploit two classes of C-type gating mechanisms. Both C-type gate rearrangements are suppressed by binding of the activator ML335 (*20*) to the K_{2P} modulator pocket in the P1-M4 interface, providing an explanation for how such compounds stabilize the activated state. Shortening the uniquely long SF2-M4 loop to match the canonical length found in the first K_{2P} pore domain (PD1) and in other potassium channels, or disrupting the conserved hydrogen bond network centered on Glu^{234} from the M3 helix that supports the SF2-M4 loop, the "M3 glutamate network" blunts C-type gate responses to various physical and chemical stimuli. Destabilization of the M3 glutamate network compromises ion selectivity but can be reversed by channel activation, indicating that loss of S1 and S2 ions and associated selectivity filter changes reduce ion selectivity, similar to other channels (*27*). Together, our data establish that C-type gating occurs through potassium-dependent order-disorder transitions in the selectivity filter and adjacent loops that respond to gating cues relayed through the SF2-M4 loop. These findings underscore the importance of the SF2-M4 loop as a conduit for signals sensed by the cytoplasmic tail and transmitted through the M4 transmembrane helix (*3*, *4*) and highlight the potential for targeting the SF2-M4 loop for the development of new, selective K_{2P} channel modulators.

RESULTS

Potassium-dependent selectivity filter structural changes

Despite the fact that C-type gating is the principal K_{2P} gating mechanism (*3*–*6*) and that previously determined K_{2P} structures show major conformational changes that affect function (*20*–*26*), all prior

[1]Cardiovascular Research Institute, University of California, San Francisco, CA 93858-2330, USA. [2]Department of Physiology, University of California, San Francisco, CA 93858-2330, USA. [3]Science Division, Diamond Light Source, Harwell Science and Innovation Campus, Didcot, OX11 0DE, UK. [4]Department of Biological Sciences, University of Pittsburgh, Pittsburgh, PA, 15260, USA. [5]Department of Pharmaceutical Chemistry, University of California, San Francisco, CA 93858-2330, USA. [6]Departments of Biochemistry and Biophysics, and Cellular and Molecular Pharmacology, University of California, San Francisco, CA 93858-2330, USA. [7]California Institute for Quantitative Biomedical Research, University of California, San Francisco, CA 93858-2330, USA. [8]Kavli Institute for Fundamental Neuroscience, University of California, San Francisco, CA, 93858-2330, USA. [9]Molecular Biophysics and Integrated Bio-imaging Division, Lawrence Berkeley National Laboratory, Berkeley, CA, 94720 USA.
*These authors contributed equally to this work.
†Present address: Department of Molecular Medicine, University of Pavia, Pavia, Italy.
‡Present address: Department of Industrial and Applied Genomics, IBM AI and Cognitive Software Organization, IBM Almaden Research Center, San Jose, CA, USA; NSF Center for Cellular Construction, University of California San Francisco, San Francisco, CA, USA.
§Corresponding author. Email: michael.grabe@ucsf.edu (M.G.); daniel.minor@ucsf.edu (D.L.M.)

K_{2P} structures show identical, canonical selectivity filter conformations and lack changes that could be attributed to C-type gating (fig. S1). Notably, these structures were all determined in the presence of 150 to 200 mM permeant ions, a condition that would be expected to confer considerable C-type gate stabilization based on functional studies (*3*, *4*, *6*, *10*). In notable contrast, structure determination of a crystallizable $K_{2P}2.1$ (TREK-1) construct, $K_{2P}2.1_{cryst}$ (*20*), under a series of seven potassium concentrations, 0, 1, 10, 30, 50, 100, and 200 mM [K^+] at resolutions of 3.9, 3.4, 3.5, 3.3, 3.6, 3.9, and 3.7 Å, respectively, revealed obvious potassium-dependent changes in the selectivity filter structure, particularly in SF2 and the SF2-M4 loop (Fig. 1A, figs. S2 and S3, and table S1). These changes manifested at potassium concentrations ≤50 mM and eventually encompassed all of the SF2-M4 loop and the upper portion of the selectivity filter (Gly^{253}-Lys^{271}) (figs. S2 and S3). Additional changes were observed in SF1 residues Gly^{144}-Asn^{147} at the lowest potassium concentrations (0 and 1 mM) (Fig. 1B and fig. S3, A and B). Structure determination under the same set of potassium concentrations in the presence of the $K_{2P}2.1$ (TREK-1) activator ML335 (*20*) at resolutions of 3.4, 2.6, 3.0, 3.2, 3.2, 3.3, and 3.8 Å, respectively, yielded essentially identical structures having canonical selectivity filter conformations at all potassium concentrations (Fig. 1, C and D, and figs. S2 and S3, A and B), a result that agrees with the ability of ML335 to activate the C-type gate directly (*20*). The observed structural changes were limited to the SF1 and SF2-M4 regions and were uncorrelated with differences in resolution (fig. S2A). Moreover, other parts of the channel remained well defined even when the SF2-M4 loop became disordered (fig. S2, B and C) and had essentially the same conformations as prior $K_{2P}2.1$ (TREK-1) structures that show the absence of an inner gate (*20*). Hence, the changes we observe clearly represent a local, specific, potassium-dependent loss of structure.

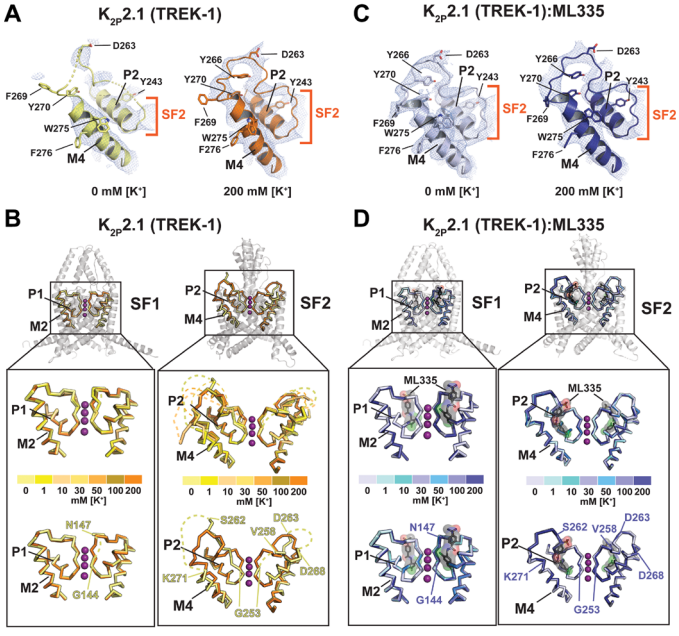

Fig. 1. $K_{2P}2.1$ (TREK-1) selectivity filter potassium-dependent conformational changes. (**A**) Exemplar 0 and 200 mM [K^+] $K_{2P}2.1$ (TREK-1) SF2 2Fo-Fc electron density (1σ). Select residues and channel elements are indicated. Dashes indicate disordered regions. (**B**) [K^+]-dependent structural changes in $K_{2P}2.1$ (TREK-1) SF1 (left) and SF2 (right). Top: Superpositions of structures determined in 0 (pale yellow), 1 (yellow), 10 (light orange), 30 (yellow orange), 50 (bright orange), 100 (olive), and 200 (orange) mM [K^+]. Bottom: Superposition of 0 and 200 mM [K^+] structures. Dashed lines indicate regions absent from the structures. Lower panel labels mark model boundaries. (**C**) Exemplar 2Fo-Fc electron density (1σ) for the $K_{2P}2.1$ (TREK-1):ML335 complex SF2 at 0 and 200 mM [K^+]. (**D**) $K_{2P}2.1$ (TREK-1):ML335 complex structural comparisons of SF1 (left) and SF2 (right). Top: Superposition of structures determined in 0 (blue white), 1 (pale cyan), 10 (aquamarine), 30 (light blue), 50 (marine), 100 (slate), and 200 (deep blue) mM [K^+]. Bottom: Superposition of 0 and 200 mM [K^+] structures. ML335 is gray and shows its molecular surface. Lower panel labels indicate the equivalent residues from (B). Potassium ions are from the 200 mM [K^+] structures and are shown as magenta spheres.

Structural studies of homotetrameric potassium channels have established the intimate connection between the presence of potassium ions in the selectivity filter and the conductive conformation in which the selectivity filter backbone carbonyls coordinate the permeant ions (*11*, *13*–*17*). Hence, we asked whether the SF1, SF2, and the SF2-M4 loop structural changes in different potassium concentrations were also accompanied by changes to the number of ions in the filter. Comparison of selectivity filter region omit maps (*28*) showed clear evidence for variation in the number of ions in the filter that paralleled the structural changes in the filter and supporting loops. The 100 and 200 mM [K^+] structures showed ions at all four selectivity filter sites, S1 to S4, similar to prior structures determined under similar conditions (*20*). Whereas in the 0, 1, 10, 30, and 50 mM [K^+] structures, the ion densities at sites S1 and S2 were clearly absent, while the S3 and S4 ions persisted to the lowest potassium concentration examined (Fig. 2A and fig. S4A). By contrast, all of the $K_{2P}2.1$ (TREK-1):ML335 structures showed ions at S1 to S4 regardless of the potassium concentration, underscoring the ability of ML335 to stabilize the filter (Fig. 2B and fig. S4B) and directly activate the C-type gate (*20*).

To confirm that the changes in the electron density reflected potassium ion occupancy and were not due to resolution differences, we used long-wavelength x-rays above and below the potassium K-absorption edge (λ = 3.3509 and 3.4730 Å) to measure potassium anomalous scattering (*29*, *30*) from crystals in 1 or 200 mM [K^+] in the absence or presence of ML335. Anomalous difference maps showed unequivocally that potassium ions occupy sites S1 to S4 under 200 mM [K^+] conditions irrespective of the presence of ML335 (Fig. 2, C and D). By contrast, the density from 1 mM [K^+] conditions showed a ML335-dependent difference in the number of potassium ions (Fig. 2, C and D) that agreed with our initial observations (Fig. 2, A and B, and table S2). In the absence of the activator, potassium ions were observed only in the lower portion of the filter, whereas potassium ions are found at all four positions in presence of ML335 (Fig. 2, C and D). Together, these data demonstrate that the loss of structure observed in the upper portion of SF2 as potassium concentrations are lowered is accompanied by a loss of potassium ions at sites S1 and S2 (Fig. 2E). Hence, the well-ordered, fully ion-bound conformations represent the active state of the filter, whereas the low [K^+] structures in the absence of ML335 that have various degrees of disorder in SF1, SF2, and the SF2-M4 loop and lack of ions at S1 and S2 reflect low activity conformations of the C-type gate. This assignment agrees with the idea that K_{2P} C-type gate activation involves a rigidification of the filter and surrounding structure (*20*).

C-type gate and connecting loops are dynamic

To gain further insight into how potassium occupancy and ML335 affect the C-type gate, particularly in the context of a lipid bilayer, we turned to molecular dynamics (MD) simulations of $K_{2P}2.1$

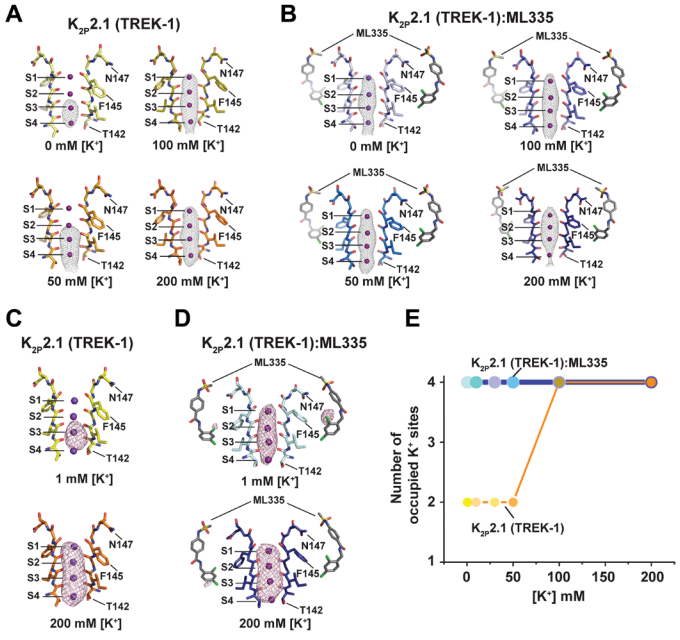

Fig. 2. $K_{2P}2.1$ (TREK-1) selectivity filter ion occupancy as a function of $[K^+]$. (**A** and **B**) Polder omit maps (*28*) for structures of (A) $K_{2P}2.1$(TREK-1) and (B) $K_{2P}2.1$(TREK-1):ML335 determined in 0 mM $[K^+]$ [pale yellow (5σ); blue white (4σ)], 50 mM K^+ [bright orange (5σ); marine (4σ)], 100 mM $[K^+]$ [olive (4σ); slate (4σ)], and 200 mM $[K^+]$ [orange (4σ); deep blue (4σ)]. Potassium ions are magenta spheres. Sites S1 to S4 are labeled. ML335 is shown as sticks. (**C** and **D**) Potassium anomalous difference maps (*29*) for (C) $K_{2P}2.1$(TREK-1) and (D) $K_{2P}2.1$(TREK-1):ML335 determined in 1 mM $[K^+]$ [yellow (4σ); pale cyan (4σ)] and 200 mM $[K^+]$ [orange (4σ); deep blue (4σ)]. In (A) and (D), SF1 in the 200 mM $[K^+]$ conformation is shown for reference. S1 to S4 sites and select amino acids are labeled. (**E**) Plot of the number of observed selectivity filter ions as a function of $[K^+]$. Colors correspond to the scheme in Fig. 1 (C and D).

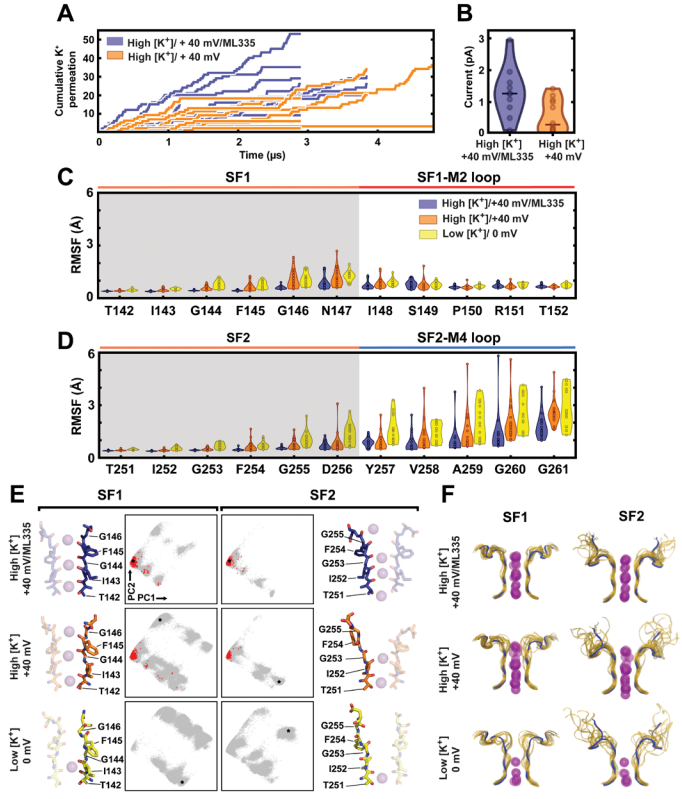

Fig. 3. $K_{2P}2.1$ (TREK-1) conductance properties and SF conformational dynamics from MD simulations. (**A**) Cumulative K^+ ion permeation events over simulation time for all individual trajectories in High $[K^+]$/+40 mV (orange) and High $[K^+]$/+40 mV/ML335 (purple) conditions. (**B**) Current calculated from the trajectories in (A). Each point shows the average current from one independent trajectory; horizontal bars indicate median. (**C** and **D**) C_α RMSF values of the filter and loop regions for (C) pore domain 1 and (D) pore domain 2, for all simulated conditions. Each point represents RMSF calculated from one $K_{2P}2.1$ (TREK-1) subunit of one trajectory. Conserved selectivity filter signature sequences are shaded gray. (**E**) PCA analysis of SF1 and SF2 dihedral angles and exemplar filter conformations. Each dot represents the instantaneous conformation of the TIGFG backbone dihedral angles from single selectivity filter. Black stars indicate the location in PC1 vs. PC2 space of the adjacent exemplar. Red dots indicate conformations immediately preceding K^+ permeation events. (**F**) Final SF1 (left) and SF2 and loop (right) ion and backbone conformations from all simulation trajectories. Transparent gold ribbons are the final frame of each trajectory; transparent purple spheres are potassium ions. Solid blue ribbons represent the initial crystal structure conformation.

(TREK-1). Initially, we simulated two conditions: (i) 180 mM $[K^+]$ and a +40-mV applied membrane potential (denoted "High $[K^+]$/+40 mV," 36.5 μs aggregate) and (ii) the same $[K^+]$ and potential with bound ML335 (denoted "High $[K^+]$/+40 mV/ML335," 31.6 μs aggregate). Both conditions showed many permeation events (144 and 253 for High $[K^+]$/+40 mV and High $[K^+]$/+40 mV/ML335, respectively), confirming that the initial structures represent conduction competent states. Nevertheless, the pattern of permeation events with respect to time showed notable differences depending on ML335 (Fig. 3A). Over the course of the simulations, most of the High $[K^+]$/+40 mV/ML335 trajectories (8 of 10) remained in a stable, ion-conducting state. By contrast, most (7 of 12) of the High $[K^+]$/+40 mV trajectories entered long-lived (>1 μs) nonconducting states from which they did not recover and that were characterized by obvious disruptions of the initial selectivity filter conformation. Concordantly, the two conditions had a substantial difference in the current (0.3 pA versus 1.3 pA for High $[K^+]$/+40 mV and High $[K^+]$/+40 mV/ML335, respectively) (Fig. 3B). There were no major changes during the simulations in the M4 helix position or in other parts of the channel outside of the selectivity filter when compared with their starting positions as defined by the crystal structures.

To determine whether there were differences in C-type gate dynamics across simulation conditions, we examined a number of factors. Because structural waters behind the selectivity filter stabilize both the active and C-type inactivated states of the model homotetrameric channel KcsA (*31*), we first characterized the role that water molecules have on the $K_{2P}2.1$ (TREK-1) filter conformation. We found that in conductive states, regardless of the presence of ML335, a characteristic water network behind the filter stabilizes SF1 and SF2 through hydrogen bonds to the backbone amides of Phe^{145}/Gly^{146} and Phe^{254}/Gly^{255}, respectively (fig. S5, A and B). As the $K_{2P}2.1$ (TREK-1) filter moves away from the canonical, conductive conformation, these well-organized networks dissolve (fig. S5C). Nevertheless, before dissolution, there were no obvious differences in the water configurations with or without ML335 that would explain the differences in conduction and filter stability. We also note that unlike in KcsA, where water molecules stabilize a discrete nonconducting pinched filter state (*11*, *14*, *31*), these $K_{2P}2.1$ (TREK-1)

nonconductive states were heterogeneous, having many different conformations of the filter and surrounding waters.

We next asked whether dynamics in the filter region could explain differences in filter stability. To do so, we calculated root-mean-square fluctuation (RMSF) values for the selectivity filter and the postfilter loops. Because the crystal structures showed that low potassium occupancy in the filter resulted in increased mobility in these regions (Figs. 1, B and D, and figs. S2A and S3), we included a third set of simulations in which $K_{2P}2.1$ (TREK-1) had only a single ion in the filter under no applied membrane potential (denoted "Low $[K^+]$/0 mV," 20.6 μs aggregate). This analysis revealed that residues Phe^{145}-Ser^{149} of SF1, Phe^{254}-Gly^{261} of SF2, and the SF2-M4 loop comprise the three most dynamic areas near the filter and showed that their mobility was greatly restricted by ML335 (Fig. 3, C and D). Further, under Low $[K^+]$/0 mV conditions, the mobility of these regions exceeded either of the High $[K^+]$/+40 mV conditions (fig. S5D). Together, the simulations indicate that the absence of K^+ in the filter versus the presence of ML335 have strong, opposite effects on the dynamics of the selectivity filter and SF2-M4 loop (Fig. 3, C and D).

To determine specific structural features associated with loss of conduction and how these features relate to the broader C-type gating context, we analyzed the backbone dihedral angles of the SF1 and SF2 ion-coordinating "TIGFG" amino acid motifs. We used a simple statistical procedure known as principal components analysis (PCA) to transform the 10 backbone dihedral angles from each TIGFG conformation into a new coordinate system wherein the greatest variance in conformations lies along the first axis (principal component), the second greatest along the second axis, and so on (*32*). Focus on the first few high-variance components provides a natural way of reducing the dimensionality of the data and reveals collective changes that cannot be gleaned from examining changes in individual dihedral angles. Projecting all simulation snapshots onto the first two principal components (PC1 and PC2) (Fig. 3E) uncovered a distinct grouping of SF1 and SF2 conformations that lack major deviations from the initial structure. All prior K_{2P} selectivity filter structures (fig. S6, A and B) (denoted as the "native state") and selectivity filters from other potassium channels thought to capture either conducting states (*14*, *33*) or, unexpectedly, C-type inactivated states (*14*, *17*), map to the center of this group (fig. S6C). Additional clustering analysis of all High $[K^+]$ selectivity filters in the PC1 to PC3 space separated out many distinct clusters of nonnative conformations in which the backbone dihedral angles deviate substantially from the native state (fig. S6D). Some of these conformations are reached from the canonical SF1 structure via a single discrete backbone "crankshaft" motion between either the S2 and S3 sites (Ile^{143}/Gly^{144}) (fig. S6D, cluster 2) or at the top of the S0 site (Gly^{146}/Asn^{147}) (fig. S6D, cluster 3) that result in a flip of the amide group plane that reorients the backbone carbonyl away from the pore and correspond to conformations suggested to be involved in C-type gating in previous K_{2P} channel simulations (*34*, *35*). The remaining SF1 and SF2 clusters represent larger deviations from the initial state and cannot be described by single amide crankshaft motions. Some of these configurations are reminiscent of the unusual selectivity filter structure of the nonselective channel NaK (fig. S6, C and D) (*36*), while others represent novel conformations that have not been observed experimentally (fig. S6D). Notably, conformations with multiple crankshaft motions and large dihedral angle changes are more highly populated in the absence of ML335 and are especially abundant under Low $[K^+]$ conditions (Fig. 3, E and F).

Of all of the $K_{2P}2.1$ (TREK-1) conformations observed under high $[K^+]$ conditions, only a few are compatible with K^+ permeation. Greater than 90% of ion conduction events occurred when all four SF strands occupied the native state conformational cluster. No conduction events were observed when more than two SF strands adopted nonnative states. Under High $[K^+]$/+40 mV/ML335 conditions, SF1 and SF2 were found in the native state cluster 90 and 95% of the time, respectively, while under High $[K^+]$/+40 mV conditions, these values dropped to 64 and 86% (Fig. 3E). Thus, the presence of ML335 reduces the accessible conformational space of the filter, restricting SF1 and SF2 largely to their native, conductive conformations. This conformational restriction causes longer periods of sustained conduction and higher current values relative to the High $[K^+]$/+40 mV condition (Fig. 3, A and B), in line with the fact that ML335 directly activates the $K_{2P}2.1$ (TREK-1) C-type gate (*20*).

In all three simulation conditions, most of the nonconductive filter conformations have multiple dihedral angle deviations from the canonical structure (Fig. 3F and fig. S6D) and share a loss of ion binding sites at S1, S2, or both due to rearrangement of the ion coordinating carbonyls (Fig. 3E, bottom and middle right, and fig. S6D). These changes leave only the S3 and S4 sites competent for potassium binding and are in excellent agreement with the crystallographic ion positions observed under low potassium conditions (Figs. 1 to 3F and figs. S2 and S3). Furthermore, examination of the ensemble of final SF1 and SF2 backbone conformations from the simulations under different conditions shows that these structural components display increased conformational disorder and pseudo-fourfold symmetry breaking that is in excellent agreement with the x-ray structures (Fig. 3F). SF1 adopts nonnative conformations, particularly around Asn^{147}, which pinch the conduction pathway, whereas SF2 preferentially dilates out of the pathway (movies S1 and S2). This asymmetry extends beyond the parts of the filter that directly contact the permeant ions. Although the SF1-M2 loop remains largely native-like, despite the changes in SF1, the longer SF2-M4 loop is highly mobile (movie S2). This later observation agrees well with the loss of density for SF2-M4 loop in the low $[K^+]$ crystal structures (Fig. 1, A and B). Together, the structures and simulations support the idea that ML335 acts by stabilizing the K_{2P} selectivity filter in a conductive state and indicate that the low $[K^+]$ crystal structures represent an inactive C-type gate in which asymmetric disorder in the extracellular portion of the selectivity filter disrupts the S1 and S2 ion binding sites and inhibits ion conduction.

ML335 stabilizes the $K_{2P}2.1$ (TREK-1) open state

Both the crystallographic and computational data strongly suggest that ML335 stabilizes the conductive state of the C-type gate. To test this idea directly, we recorded $K_{2P}2.1$ (TREK-1) single channels alone and in the presence of ML335 (Fig. 4, A and B). ML335 activated the channels in the same way regardless of whether it was applied to the bath (Fig. 4A) or through the pipette (Fig. 4B). The effect of bath application was apparent in ~15 min, whereas the pipette application had immediate effects in line with the fact that the K_{2P} modulator pocket faces the extracellular solution. The data clearly show that in both cases, ML335 increases channel open probability but not the single-channel conductance (Fig. 4, C to E). By contrast, the activator BL-1249, which is thought to act by a mechanism different from that of the K_{2P} modulator pocket activators ML335 and ML402 (*37*, *38*), increases both open probability and single-channel conductance (*38*). The clear effects of ML335 on channel open probability

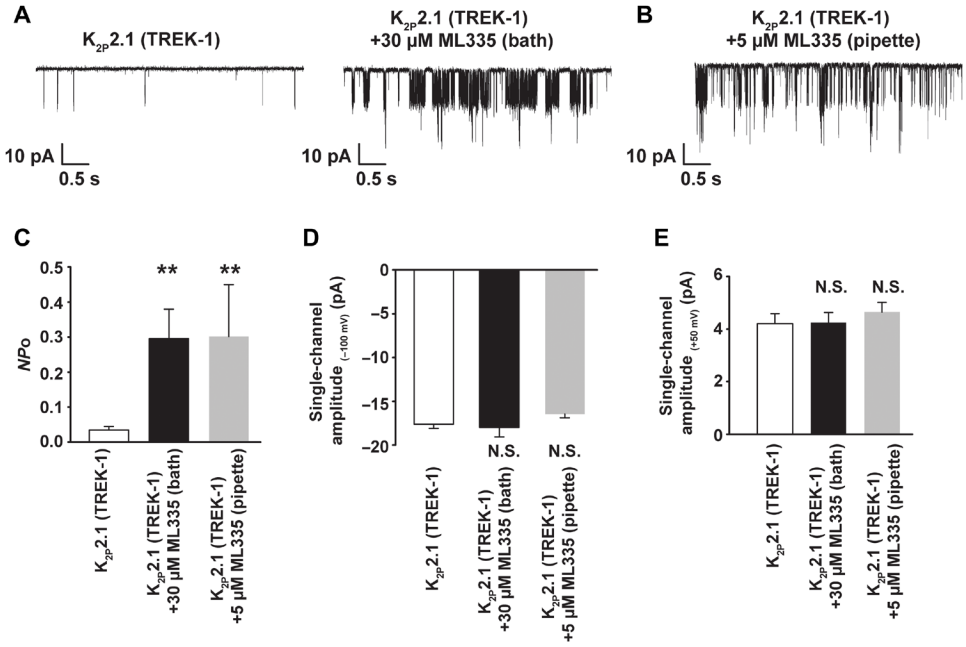

Fig. 4. Effects of ML335 on K_{2P}2.1 (TREK-1). (**A**) Exemplar K_{2P}2.1 (TREK-1) single-channel recordings at −100 mV before (left) and after (right) application of 30 μM ML335 to the same cell-attached patch. (**B**) Exemplar K_{2P}2.1 (TREK-1) single-channel recordings at −100 mV in the presence of 5 μM ML335 applied in the pipette solution of a cell-attached patch. (**C**) Open channel probability at −100 mV from single-channel analysis calculated on recordings of ≥30-s duration. (**D** and **E**) Single-channel amplitude at (D) −100 mV and (E) +50 mV. Error bars indicate SEM ($n = 5$ to 7). "**" indicates $P < 0.01$ and "N.S." indicates not statistically different relative to K_{2P}2.1 (TREK-1).

match the expectations from the crystallographic and computational observations that show that ML335 stabilizes the ion-filled conductive state of the selectivity filter C-type gate (Figs. 1 to 3) and support the idea that rigidification of the P1-M4 interface, comprising the K_{2P} modulator pocket, is central to C-type gate activation of K_{2P}s (*20*).

The SF2-M4 loop integrates responses from diverse gating cues

In most potassium channels, including the first K_{2P} pore domain (PD1), a six-residue loop connects the extracellular end of the selectivity filter to the outer transmembrane helix of the pore domain (Fig. 5, A and B, and fig. S7A, and B). K_{2P}s are unique in that the second pore domain loop (PD2) is longer than this canonical length by six to eight residues in 14 of the 15 K_{2P} subtypes (fig. S7, C and D). Despite these differences, the N-terminal portions of the PD1 and PD2 loops adopt very similar structures up to Pro^{150} and Ala^{259}, respectively (Fig. 5A). The simulations revealed that loss of SF2-M4 loop stability was accompanied by the disruption of a hydrogen bonding network, the Glu^{234} network, at the C-terminal end of the PD2 linker involving the M3 Glu^{234} carboxylate, the SF2-M4 loop Gly^{260} backbone amide, and the M4 Tyr^{270} phenolic ─OH (Fig. 5, C and D). Binding of ML335 to the K_{2P} modulator pocket stabilizes the SF2-M4 loop from the opposite side of the Glu^{234} network (Fig. 5C), increases the strength of the Glu^{234} hydrogen bonding network in the simulations (fig. S7, E and F), and strongly attenuates potassium-dependent loop dynamics (Figs. 1, B to D, and 3, C and D; and figs. S2 and S3). Conversely, in low $[K^+]$ simulations, the Glu^{234} network is disrupted (figs. S7, E and F), and loop dynamics are enhanced (Fig. 3D). Together, these results suggest that loop dynamics are important for C-type gating, with Glu^{234} playing a key role by supporting the SF2-M4 loop structure. Notably, the equivalent position of the K_{2P} PD1 outer helix, M1 also has a highly conserved glutamate (fig. S7G) that affects C-type gating through interactions with the short SF1-M2 loop (*10*, *39*) in a manner that is conserved with voltage-gated potassium channels (*40*, *41*). Therefore, given the indications from our structures and simulations that Glu^{234} network integrity should be important for gating, we set out to test consequences of restricting the SF2-M4 loop mobility and disrupting the Glu^{234} network.

To create a channel having symmetric length loops between each selectivity filter and its outer transmembrane helix, we transplanted Pro^{150}-Gly^{155} from PD1 onto PD2, denoted "$Loop2_{Sym-6}$" (Fig. 5B). $Loop2_{Sym-6}$ showed blunted responses to temperature (Fig. 5, E and F) and pressure (Fig. 5, G and H). Consistent with the deletion of key ML335-binding SF2-M4 loop residues, $Loop2_{Sym-6}$ was unresponsive to ML335 (Fig. 5, I and J) but remained partially sensitive to BL-1249 (Fig. 5, K and L), an activator that affects the channel from a site under the selectivity filter (*37*, *38*). Measurement of rectification in inside-out patches, a parameter that is a direct measure of C-type gate activation (*5*, *20*), demonstrated that unlike gain-of-function mutants (*20*), $Loop2_{Sym-6}$ does not have a constitutively activated C-type gate that would render it insensitive to gating commands (fig. S8, A and B). Hence, the blunted responses caused by shortening the SF2-M4 loop to the canonical length indicate that the unusual length of the SF2-M4 loop is central to C-type gate control.

Disruption of the Glu^{234} hydrogen bond network by E234Q and Y270F mutations resulted in channels having severely blunted responses to temperature (Fig. 5, E and F), pressure (Fig. 5, G and H), ML335 (Fig. 5, I and J), and BL-1249 (Fig. 5, K and L). Unlike $Loop2_{Sym-6}$, both mutations compromised ion selectivity as evidenced by an altered reversal potential (Fig. 5, E, G, I, and K, and fig. S9). This baseline selectivity defect was partially corrected by temperature or pressure activation (Fig. 5, E and G, and fig. S9). Inside-out patch clamp experiments demonstrated that neither mutant resulted in channels having a C-type gate that was activated

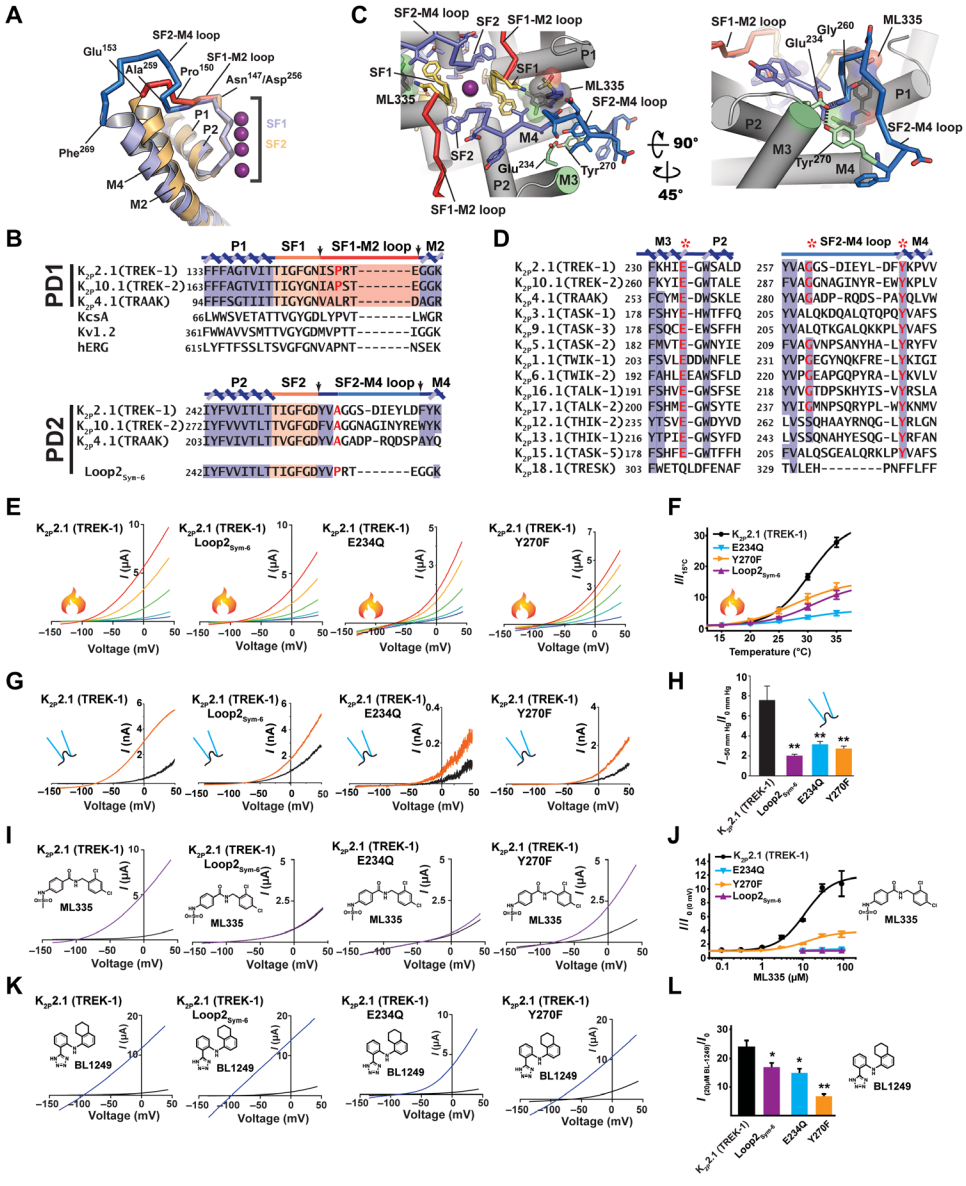

Fig. 5. K_{2P} SF2-M4 loop is central to C-type gate function. (**A**) K_{2P}2.1 (TREK-1) P1-SF1-M2 (orange) and P2-SF2-M4 (slate) superposition. SF1-M2 loop (red) and SF2-M4 loop (blue) and portions having a shared conformation (dark blue) are indicated. Residue labels indicate the SF1-M2 and SF2-M4 loop ends and structural divergence point (Pro150/Ala259). (**B**) Sequence comparison. Arrows denote selectivity filter–outer transmembrane helix linker ends. Red indicates Pro150/Ala259 equivalents. (**C**) K_{2P}2.1 (TREK-1):ML335 complex SF2-M4 loop details. SF1 (yellow), SF2 (slate), SF1-M2 (red), and SF2-M4 (marine) are indicated. Conserved Glu^{234} (green), Tyr^{270} (green), Gly^{260} (marine) hydrogen bond network is indicted. ML335 is shown as sticks and space filling. (**D**) Human K_{2P} channel M3 glutamate network conservation (red and asterisks). Figure S7 has sequence codes. (**E**) Exemplar two electrode voltage clamp (TEVC) recordings at 15°C (blue), 20°C (light green), 25°C (lime green), 30°C (orange), and 35°C (red). (**F**) Normalized temperature responses ($n \geq 10$). (**G**) Exemplar inside-out pressure response at 0 mmHg (black) and 50 mmHg (orange). (**H**) Averaged pressure responses ($n \geq 4$). (**I**) Exemplar TEVC recordings for 30 μM ML335 (purple) activation. (**J**) ML335 dose-response curves ($n \geq 3$). EC_{50} 11.3 ± 3.4 and 12.7 ± 4.1 μM, maximum activation 11.9 ± 1.3, and 3.8 ± 0.4 fold for K_{2P}2.1 (TREK1) and K_{2P}2.1 (TREK1) Y270F, respectively. (**K**) Exemplar TEVC recordings for 20 μM BL-1249 (blue) activation. (**L**) Normalized responses to 20 μM BL-1249 (n ≥ 7). (F), (H), (J), and (L) show K_{2P}2.1 (TREK1) (black), K_{2P}2.1 (TREK1) $Loop2_{sym6}$ (purple), K_{2P}2.1 (TREK1) E234Q (light blue), and K_{2P}2.1 (TREK1) Y270F (orange). "*" and "**" indicate $P < 0.05$ and $P < 0.001$, respectively.

at rest, although Y270F caused a slight decrease of the rectification coefficient (fig. S8, A and B). Unexpectedly, we also found that E234Q exhibited a time- and voltage-dependent inactivation (fig. S8, C and D), further validating the importance of the Glu^{234} network for C-type gate control. Together, with prior mutational studies suggesting a role for the SF2-M4 loop in external pH gating (*42*), these data strongly support the key role that the SF2-M4 loop has in K_{2P} channel gating and underline the importance of SF2-M4 stabilization by the network centered on Glu^{234}.

The M3 glutamate network has a conserved role in C-type gate control

The key elements of the Glu^{234} network are highly conserved among K_{2P}s (Fig. 5D). To test its general importance, we disrupted this

network in K_{2P}3.1(TASK-1), a K_{2P} from a subfamily distant from K_{2P}2.1 (TREK-1) (*2*). Structural comparison shows that K_{2P}3.1(TASK-1) Glu^{182}, Leu^{208}, and Tyr^{220} form a network similar to the K_{2P}2.1 (TREK-1) Glu^{234}-Gly^{260}-Tyr^{270} network (fig. S10A). Notably, this network is structurally conserved although K_{2P}3.1(TASK-1) has one of the longest SF4-M4 loops (14 residues) (Figs. 5D and fig. S7D) and has a large sidechain, leucine, at the position that contributes the backbone amide (Fig. 5, C and D). Disruption of this network in K_{2P}3.1(TASK-1) had substantial functional consequences. K_{2P}3.1(TASK-1) E182Q failed to produce functional channels (fig. S10C), whereas K_{2P}3.1(TASK-1) Y220F yielded channels that were more readily closed by low pH (fig. S10, D and E). This result phenocopies disruption of interactions on the opposite side of the SF2-M4 loop in P1-M4 interface by the K_{2P}3.1(TASK-1) I88G mutant (*3*) and indicates that the Y220F mutation destabilized the SF2-M4 loop and C-type gate. Together, our data demonstrate that the Glu^{234} network and its stabilization of the SF2-M4 loop is a central element of C-type gate control. Because of its conservation and functional importance in diverse K_{2P}s, we term this network as the M3 glutamate network.

DISCUSSION

Mechanistic implications for K_{2P} channel function

Despite the central role of the selectivity filter C-type gate in K_{2P} channel function (*3*–*6*), observation of conformational changes that would provide a framework for understanding the principles of K_{2P} C-type gating has eluded previous structural studies (*20*–*26*, *43*). Our data establish that control of the K_{2P} C-type gate involves unprecedented, asymmetric, potassium-dependent, order-disorder transitions in the selectivity filter and surrounding loops (Figs. 1 and 6). The selectivity filter conformational changes associated with K_{2P} C-type gating comprise two classes of rearrangements that eliminate the S1 and S2 ion binding sites (Fig. 6 and movies S3 and S4). One pinches the SF1 extracellular side and exposes the Asn^{147} sidechains to the extracellular solution (Fig. 6A and movie S3), a position that modulates C-type inactivation in homotetrameric potassium channels (*44*, *45*) and that undergoes similar changes in human *Ether-à-go-go*-Related potassium channel (hERG) simulations (*46*). Hence, this class of C-type gating mechanism is shared with other potassium channels. The second unwinds SF2 and the SF2-M4 loop, dilates the selectivity filter along the SF2 axis (Fig. 6B and movie S4), depends on the structure of the uniquely long K_{2P} SF2-M4 loop, and is unlike any of the prior structural changes associated with C-type gating (*20*–*26*, *43*). SF1 pinching and SF2 dilation are not mutually exclusive and are likely to be interdependent given the role of the SF ions in stabilizing the filter. Such asymmetric changes could contribute to the bimodal distribution of closed state dwell times reported for K_{2P}2.1-(TREK-1) (*47*) and the closely-related K_{2P}10.1 (TREK-2) (*48*). Further, as K_{2P} heterodimer formation yields channels having two unique SF1-M2 and SF2-M4 loops, this structural diversification together with the two nonmutually exclusive inactivation modes likely provides a mechanism for the emergence of heterodimer properties that differ from either homodimer parent (*49*–*56*). The structural rearrangements in the pore and surrounding regions, loss of S1 and S2 ions, and the demonstration that destabilization of the SF2-M4 loop structure compromises ion selectivity are reminiscent of studies of the nonselective bacterial channel NaK, which has only the S3 and S4 sites and can be converted into a potassium-selective channel by

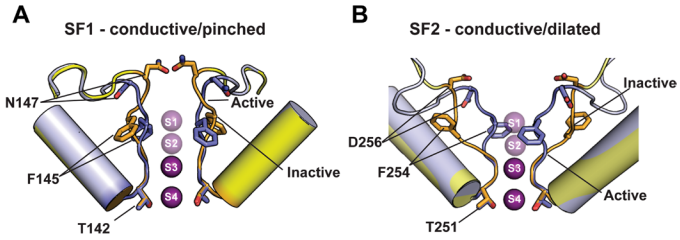

Fig. 6. Structural changes associated with C-type gating. (**A**) SF1 and (**B**) SF2 selectivity filter changes between the active (slate) [(A) and (B) conductive] and inactive (yellow orange) [(A) pinched and (B) dilated] conformations based on the 1 mM [K^+] and 0 mM [K^+]:ML335 structures, respectively. Selectivity filters for 1 mM [K^+] and 0 mM [K^+]:ML335 show select residues. Potassium ions are magenta spheres.

forming the S1 and S2 ion binding sites (*27*). Further, the loss of ion selectivity associated with K_{2P} C-type gating (*4*, *10*, *57*) and the strong link between K_{2P} gating and external potassium concentration (*3*, *4*, *6*, *10*) are in good accord with the structural and functional changes we observe.

Although C-type gating is an important mode of channel regulation in many potassium channel classes (*38*), structural insights into its mechanistic basis are limited to studies of a small number of homotetrameric potassium channel types (*11*, *13*–*19*) and lack consensus (*12*), even for the best studied example, KcsA (*58*–*61*). Nevertheless, our studies identify a unifying feature shared between K_{2P} C-type gating and homotetrameric potassium channel C-type gating—the importance of the conserved glutamate at the extracellular end of the pore module outer helix (Figs. 5, C and D, and fig. S7G). This site on the K_{2P} PD1 M1 helix affects C-type gating through interactions with the SF1-M2 loop (*10*, *39*) similar to other channels having a canonical six residue loop between the selectivity filter and pore module outer helix (Fig. 5B) (*40*, *41*, *62*). The equivalent PD2 glutamate on K_{2P}21 (TREK-1) M3, Glu^{234}, forms a conserved network together with a M4 tyrosine, Tyr^{270}, the M3 glutamate network that supports the uniquely long SF2-M4 loop found throughout the K_{2P} family (fig. S7D). Disruption of the M3 glutamate network blunts responses to diverse stimuli in distantly related K_{2P}s (Fig. 5 and figs. S9 and S10) and establishes that, together with its role in external pH responses (*42*), the SF2-M4 loop is a hub that integrates chemical and physical gating cues sensed in other parts of the channel (Fig. 5, E to L) and relayed to the filter via M4 (*3*, *4*). The M3 glutamate network is conserved in every functional K_{2P} except K_{2P}18.1 (TRESK), the only K_{2P} having a short SF2-M4 loop (Fig. 5D and fig. S7D). This conservation, together with the report that a pulmonary hypertension mutation at the conserved M3 glutamate in K_{2P}3.1 (TASK-1), E182K, disrupts function (*63*) underscores the importance of the M3 glutamate network and SF2-M4 loop in gating throughout the K_{2P} family.

Our studies establish that K_{2P} channel C-type gating entails filter pinching (SF1) and pore dilation (SF2), highlight the dynamic nature of C-type inactivated states (*20*, *64*), and indicate that the innate heterodimeric nature of the K_{2P} filter architecture enables two general C-type gating mechanisms, pinching and dilation (*12*), which have been viewed as mutually exclusive, to operate in one channel. The substantial differences in the degree of conformational changes between SF1 and SF2 appear to depend on the loop length connecting these elements to the outer transmembrane helix of their respective pore domains. Binding of small molecules, such as ML335, to the K_{2P} modulator pocket enables conduction by stabilizing the SF2-M4

loop and selectivity filter and increasing channel open probability, whereas disruption of the integrity of the SF2-M4 loop blunts transduction of gating cues that originate from the intracellular C-terminal tail (*3*, *65*–*70*) and pass through M4 to the C-type gate (*3*, *4*). These findings corroborate the ideas that the K_{2P} selectivity filter and its supporting architecture are dynamic under basal conditions (*20*), that ion permeation requires limiting filter mobility through ligand binding to the K_{2P} modulator pocket or by conformational changes transmitted through the M4 helix (*20*), that permeant ions organize and stabilize the K_{2P} conductive state (*5*, *38*), and that the inactive state involves an ion-depleted filter (*5*). Further, our observation that the filter can adopt nonconductive conformations although the M4 transmembrane helix is in the "up" position underscores previous studies indicating that M4 conformation is not the sole determinant of K_{2P} activation (*20*, *71*). The key role for the SF2-M4 loop in transducing gating cues sensed by intracellular channel components to the K_{2P} selectivity filter gate such as temperature and pressure (Fig. 5, E to H), as well as external pH responses (*42*), demonstrates its pivotal function in K_{2P} gating. These properties, together with the ability of ML335 to increase open probability by stabilizing this loop (Figs. 1 to 5), explain why the P1-M4 interface, which is framed on one side by the SF2-M4 loop, is central to K_{2P} gating (*3*, *4*, *20*) and why small molecules bound to this interface activate the channel (*20*). These findings emphasize the potential for targeting this unique K_{2P} loop for selective small molecule or biologic modulators directed at K_{2P}-dependent processes such as anesthetic responses (*72*, *73*), pain (*74*–*76*), arrhythmia (*77*), ischemia (*72*, *78*), and migraine (*52*).

MATERIALS AND METHODS

Protein expression and purification

An engineered mouse $K_{2P}2.1$ (TREK-1), denoted $K_{2P}2.1_{cryst}$, encompassing residues 21 to 322 and bearing the following mutations: K84R, Q85E, T86K, I88L, A89R, Q90A, A92P, N95S, S96D, T97Q, N119A, S300A, E306A, a C-terminal green fluorescent protein (GFP), and His_{10} tag was expressed and purified from *Pichia pastoris* as previously described (*20*).

Crystallization and refinement

Purified $K_{2P}2.1_{cryst}$ was concentrated to 6 mg ml^{-1} by centrifugation (Amicon Ultra-15, 50 kDa molecular mass cutoff; Millipore) and crystallized by hanging-drop vapor diffusion at 4°C using a mixture of 0.2 μl of protein and 0.1 μl of precipitant over 100 μl of reservoir containing 20 to 25% polyethylene glycol 400 (PEG400), 200 mM KCl, 1 mM $CdCl_2$, and 100 mM Hepes (pH 8.0). Crystals appeared in 12 hours and grew to full size (200 to 300 μM) in about 1 week.

Crystals were harvested and cryoprotected with buffer D [200 mM KCl, 0.2% octyl glucose neopentyl glycol (OGNG), 15 mM n-heptyl-β-D-thioglucoside (HTG), 0.02% cholesteryl hemisuccinate (CHS), 1 mM $CdCl_2$, and 100 mM Hepes (pH 8.0)] with 5% step increases of PEG400 up to a final concentration of 38%. After cryoprotection, crystals were incubated for 8 hours in buffer E [38% PEG400, 0.2% OGNG, 15 mM HTG, 0.02% CHS, 1 mM $CdCl_2$, and 100 mM Hepes (pH 8.0)] containing 200 mM salt consisting of NaCl and KCl in varied proportions to yield the following K^+ concentrations: 0, 1, 10, 30, 50, 100, and 200 mM. In the soaking experiments where the activator was present, ML335 was added to the soaking cocktail to a 1 mM final concentration. The nominal K^+ concentration in the 0 mM condition is ~20 nM. Crystals were subsequently harvested and flash-frozen in liquid nitrogen.

Datasets for $K_{2P}2.1_{cryst}$ in the presence of differing potassium concentrations, alone or with ML335, were collected at 100 K using synchrotron radiation at advanced photon source (APS) GM/CAT beamline 23-IDB/D Chicago, Illinois, processed with XDS (*79*), scaled, and merged with Aimless (*80*). Final resolution cutoffs were 3.9, 3.5, 3.4, 3.3, 3.6, 3.9, and 3.7 Å for $K_{2P}2.1_{cryst}$ in the presence of 0, 1, 10, 30, 50, 100, and 200 mM potassium, respectively, and were arrived at using the $CC_{1/2}$ criterion and standard best practices based on map quality (*81*). Final resolution cutoffs for the $K_{2P}2.1_{cryst}$:ML335 complex were 3.4, 2.6, 3.0, 3.2, 3.2, 3.3, and 3.8 Å in the presence of 0, 1, 10, 30, 50, 100, and 200 mM potassium, respectively. Structures were solved by molecular replacement using the $K_{2P}2.1_{cryst}$ structure [Protein Data Bank (PDB): 6CQ6] (*20*) as search model purged of all the ligands. The best resolution structure (1 mM:ML335) had density for head group of the lipid in the phosphatidylinositol 4,5-bisphosphate (PIP_2) binding site and was built accordingly. Several cycles of manual rebuilding, using COOT (*82*), and refinement using REFMAC5 (*83*) and PHENIX (*84*) were carried out to improve the electron density map. Twofold local automatic noncrystallographic symmetry restraints were used during refinement.

Two potassium ions were modeled into 2Fo-Fc densities of the Apo $K_{2P}2.1_{cryst}$ 0, 1, 10, and 50 mM structures; whereas, four potassium ions were modeled into 2Fo-Fc densities of the Apo $K_{2P}2.1_{cryst}$ 100 and 200 mM structures. Four potassium ions were modeled for all the $K_{2P}2.1_{cryst}$:ML335 complexes. To validate the presence of the potassium ions, a polder map (*28*) was generated for each structure. The polder map of the Apo $K_{2P}2.1_{cryst}$ 50 mM structure showed a density in the filter that extended beyond the S3 site into the S2 site; however, modeling an additional low occupancy K^+ ion at this site did not improve the overall statistics. Attempts to refine the occupancy of this third ion using PHENIX (*84*) yielded an ion having zero occupancy. Hence, the final structure has two ions in the filter, although there may be a low occupancy ion present that is not accountable due to the resolution limit of the data. The final cycle of refinement of each structure was carried out using BUSTER (*85*).

K^+ anomalous data collection

Long-wavelength data were collected at beamline I23, Diamond Light Source (*30*), UK, at a temperature ~ 50 K at wavelengths of 3.3509 and 3.4730 Å, above and below the potassium K absorption edge, processed and scaled with XDS/XSCALE (*79*). Anomalous difference Fourier maps to locate the potassium positions were calculated with ANODE (*86*) using the $K_{2P}2.1$ (TREK-1) structure (PDB:6CQ6) (*20*). Peaks present in the maps above but absent in the maps below the absorption edge were assigned as potassium.

Two-electrode voltage-clamp electrophysiology

Two-electrode voltage-clamp recordings were performed on defolliculated stage V to VI *Xenopus laevis* oocytes 18 to 48 hours after microinjection with 1 to 40 ng of mRNA. Oocytes were impaled with borosilicate recording microelectrodes (0.3- to 3.0-MΩ resistance) backfilled with 3 M KCl. Except where otherwise indicated, recording solution was 96 mM NaCl, 2 mM KCl, 1.8 mM $CaCl_2$, and 1.0 mM $MgCl_2$, buffered with 5 mM Hepes at pH 7.4 and was perfused by gravity. For pH_o experiment solutions, the standard buffer was replaced with 10 mM tris (pH 9.0 and 8.1), 5 mM Hepes (pH 7.8 and 7.1), or 5 mM MES (pH 6.5 and 5.9).

Currents were evoked from a −80-mV holding potential followed by a 300-ms ramp from −150 to +50 mV. Data were acquired using a GeneClamp 500B amplifier (MDS Analytical Technologies) controlled by pCLAMP software (Molecular Devices) and digitized at 1 kHz using Digidata 1332A digitizer (MDS Analytical Technologies).

For temperature experiments, recording solutions were heated by an SC-20 in-line heater/cooler combined with an LCS-1 liquid cooling system operated by the CL-100 bipolar temperature controller (Warner Instruments). Temperature was monitored using a CL-100–controlled thermistor placed in the bath solution 1 mm upstream of the oocyte. For temperature experiments, perfusate was warmed from 15° to 35°C in 5°C increments, with recordings performed once temperature readings stabilized at the desired values. Temperature response data were fit with the equation $A = A_{min} + (A_{max} - A_{min})/(1 + e^{(T_{\frac{1}{2}} - T)/S})$ where A_{min} and A_{max} are the minimum and maximum activation, respectively, $T_{1/2}$ is the temperature of half maximal activation, and S is the slope factor (*4*). For pH_o experiments, solutions were exchanged consecutively from 9.0 to 5.9 while maintaining the temperature at 22.5°C. pH response data were fit with the equation $A = A_{min} + (A_{max} - A_{min})/(1 + ([H^+]_o/K_{1/2})^H)$ where A_{min} and A_{max} are the minimum and maximum activation, respectively, $K_{1/2}$ is the half maximal inhibitory concentration of extracellular protons, and H is the Hill slope.

Dose-response experiments were conducted at room temperature (22°C) and used standard recording solution at pH 7.4 supplemented with 0.2% dimethyl sulfoxide and the indicated concentration of ML335 (*20*). Dose-response data were fit with the equation $A = A_{min} + (A_{max} - A_{min})/(1 + (EC_{50}/[ML335])^H)$ where A_{min} and A_{max} are the minimum and maximum activation, respectively, EC_{50} is the half maximal effective concentration, and H is the Hill slope. Data analysis and curve fitting were performed using Clampfit and Python according to procedures adapted from (*4*, *20*). *X. laevis* oocytes were harvested from female *X. laevis* according to UCSF Institutional Animal Care and Use Commitee (IACUC) Protocol AN178461.

Patch clamp electrophysiology

Human embryonic kidney cells (HEK293) were grown at 37°C under 5% CO_2 in a Dulbecco's modified Eagle's medium supplemented with 10% fetal bovine serum, 10% L-glutamine, and antibiotics [penicillin (100 IU ml^{-1}) and streptomycin (100 mg ml^{-1})]. Cells were transfected (in 35-mm-diameter wells) using Lipofectamine 2000 (Invitrogen) and a pIRES-GFP (Invitrogen) plasmid vector into which the gene encoding for mouse $K_{2P}2.1$ (TREK-1) wild type or mutants has been inserted in the first cassette (*4*). DNA (1 μg) was used for $K_{2P}2.1$ (TREK-1) and Loop2-sym-6, whereas 3 μg of DNA was necessary to record reliable currents from E234Q and Y270F. For single-channel experiments, 0.05 to 0.1 μg of DNA was used for $K_{2P}2.1$ (TREK-1). Transfected cells were identified visually using the GFP expressed in the second cassette of the pIRES-GFP plasmid vector. After a minimum of 6 hours after transfection, cells were plated onto coverslips coated with Matrigel (BD Biosciences). Data acquisition was performed using pCLAMP 10 (Molecular Devices) and an Axopatch 200B amplifier (Molecular Devices).

The inside-out configuration of the patch clamp technique was used to record K^+ or Rb^+ currents at room temperature (23° ± 2°C) 24 to 48 hours after transfection (*5*, *20*). Pipettes were pulled from borosilicate glass capillaries (TW150F-3, World Precision Instruments) and polished (MF-900 microforge, Narishige) to obtain 1- to 2-MΩ resistances.

Stretch activation of $K_{2P}2.1$ (TREK-1) and mutants was performed by applying a −50-mmHg pressure to the inside-out patch through a high-speed pressure clamp (HSPC-1, ALA Scientific Instruments) connected to the electrode suction port, after recording the current at 0 mmHg. Pipette solution contained 150 mM NaCl, 5 mM KCl, 1 mM $CaCl_2$, 2 mM $MgCl_2$, and 20 mM Hepes (pH 7.4 with NaOH). Bath solution contained 145 mM KCl, 3 mM $MgCl_2$, 5 mM EGTA, and 20 mM Hepes (pH 7.2 with KOH) and was continuously perfused at 200 ml $hour^{-1}$ during the experiment. $K_{2P}2.1$ (TREK-1) currents were elicited by a 1-s ramp from −140 to +50 mV from a −80-mV holding potential.

Single-channel activity was recorded under the cell-attached configuration of the patch clamp technique, using patch pipettes of about 8 MΩ pulled from quartz glass capillaries (QF100-70-7.5, Sutter Instrument, Novato, CA, USA) in a laser-based micropipette puller (P-2000, Sutter Instrument). Both the pipette and bath solutions contained 150 mM KCl, 5 mM EGTA-K, 1 mM EDTA-K, and 10 mM Hepes (pH 7.3 with KOH). Currents were low-pass–filtered at 2 kHz and digitized at a sampling rate of 20 kHz. Threshold detection of channel openings was set at 50%. Channel activity (*NPo*, where *N* is the number of channels in the patch and *Po* is the probability of a channel being open) was determined from ≥30 s of current recordings.

Voltage-dependent activation and inactivation of $K_{2P}2.1$ (TREK-1) and mutants were recorded from inside-out patches. Pipette solution contained 150 mM KCl, 3.6 mM $CaCl_2$, and 10 mM Hepes (pH 7.4 with KOH). Bath solution contained 150 mM RbCl, 2 mM EGTA, and 10 mM Hepes (pH 7.4 with RbOH) and was continuously perfused at 200 ml $hour^{-1}$ during the experiment. For voltage-dependent activation, currents were elicited by voltage steps from −100 to +100 mV, from a −80-mV holding potential. For voltage-dependent inactivation, currents were elicited by prepulse voltage steps from −50 to +90 mV from a −80-mV holding potential, each step being followed by a test pulse at +100 mV. All electrophysiology data were analyzed using Clampfit 10.7 (Molecular Devices).

Molecular dynamics

Simulation setup

Initial $K_{2P}2.1$ (TREK-1) simulations in the absence of ML335 were initiated from PDB:5VK5. Later simulations were based on PDB:6CQ6 (*20*), which is indistinguishable from PDB:5VK5 except for a minor difference in the C-terminal portion of M4. Simulations in complex with ML335 were constructed from PDB:6W8C. In both cases, models consisted of residues 35 to 321, a disulfide bond was formed between C93 in one subunit with C93 in the other, missing loops were built with RosettaRemodel (*87*), and N and C termini were capped with methylamide and acetyl groups, respectively. All residues were assigned their standard protonation states at pH 7. Structures were embedded in pure 1-palmitoyl-2-oleoyl-glycero-3-phosphocholine (POPC) or POPC + 4% inner leaflet mole fraction 1-stearoyl-2-arachidonoyl-glycero-3-phosphatidylinositol 4,5-bisphosphate (18:0-20:4) PIP_2 bilayers using CHARMM-GUI (*88*) and solvated in 180 mM $[K^+]$ with neutralizing Cl^- (excepting low $[K^+]$ simulations, which contained only 4 mM $[K^+]$). Two structural water molecules were added per subunit in the cavity between SF2 and pore helix 2 on the basis of water molecules identified in $K_{2P}4.1$ (TRAAK) PDB:4I9W (*23*). For simulations containing PIP_2, an additional PIP_2 lipid per channel subunit was placed in the lipid binding site adjacent to the M4 helix, as observed in the ML335:1 mM $[K^+]$ structure (PDB:6W8C). Extensive

preliminary K_{2P} simulations were initiated from a range of filter ion configurations in the S1 to S4 sites including alternating K^+ and water with waters at either S1/S3 or S2/S4, all K^+, or all K^+ with empty sites at S2 or S3. In all cases, the configuration with ions in S1/S2/S4, and an empty S3 was frequently visited during the conduction cycle. Thus, all high [K^+] simulations presented here were equilibrated with this configuration. Low [K^+] simulations were initiated with a single ion in the selectivity filter placed at the S2, S3, or S4 site. The force fields used for protein, lipids, water, and ML335 were CHARMM36m (*89*), CHARMM36 (*90*), TIP3P (*91*), and CGenFF 3.0.1 (*92-94*), respectively. Standard CHARMM parameters were used for ions (*95*).

Simulation details

Production data were collected on two platforms: Anton2 (*96*) at the Pittsburgh Supercomputing Center and local graphical processing unit (GPU) resources using GROMACS 2018 (*97*) (see table S3 for a full list). All systems were energy minimized for 8000 steps with 5 kcal/mol per $Å^2$ harmonic restraints on all protein heavy atoms, followed by a multistep equilibration in which protein restraints were gradually reduced over 10 to 12 ns. Next, for systems simulated under a membrane potential, we performed a 10-mV voltage jump every 5 ns until reaching 40 mV using the constant electric field protocol where $E_{applied} = V/L_z$ (*98*). On average L_z = 121 Å in our systems, and the final applied electric field was 0.0076 kcal/mol·Å·e. Note that systems destined for Anton2 were equilibrated with NAMD 2.13 (*99*). Production run details varied by hardware. Simulations on Anton2 used a 2.5-fs time step, an Martyna-Tobias-Klein barostat (*100*) with semi-isotropic pressure control at 1 atm, and a Nose-Hoover thermostat (*101*, *102*) with a temperature of 303.15 K. In addition, nonbonded interactions were cut off at 10 Å, long-range electrostatic interactions were calculated using the Gaussian split Ewald method (*103*), and hydrogens were constrained with SHAKE (*104*). Meanwhile, GROMACS 2018 runs used either a 2- or 2.5-fs time step, a Parrinello-Rahman barostat (*105*, *106*) with semi-isotropic pressure control at 1 atm, and a Nose-Hoover thermostat set to 310 K. Nonbonded interactions were cut off at 12 Å with force-switching between 10 and 12 Å, long-range electrostatics were calculated with particle mesh Ewald (*107*), and hydrogens were constrained with the LINCS algorithm (*108*). For low [K^+] simulations, solution ions were excluded from the selectivity filter using a flat bottom restraint on Anton2 or harmonic positional restraints in GROMACS 2018.

Simulation analysis

Ions were tracked within a 22-Å-long cylindrical volume centered on the selectivity filter, and a permeation event was recorded when an ion originating below (above) the midplane of the filter (defined by the plane separating S2 to S3 sites) exited the top (bottom) of the cylinder. The time of the permeation event was recorded as the last time the ion crossed the midplane before exit from the cylinder. PCA was carried out on the backbone dihedral angles of selectivity filter residues (142 to 146 in SF1 and 251 to 255 in SF2) as described in (*32*), and each strand was treated independently. Formation of hydrogen bonds to carboxylate or carbonyl oxygens was determined on the basis of the H to O distance (>2.5 Å for OH donors, >2.75 Å for NH donors) and C═O H angle >110°. For all analyses, conformations were sampled from the trajectories every 480 to 500 ps. All analysis code was built on top of the MDAnalysis Python package (*109*).

Statistical tests

For datasets were significance is indicated, a normality test was performed with a Shapiro-Wilk test, followed by an equality of variances test using a Levene's test. For samples with similar variances, significance was evaluated using either a paired or unpaired Student's *t* test. For data that were not normally distributed, a nonparametric Mann-Whitney test or a Wilcoxon signed-rank test for paired analyses was used. For samples with unequal variance, significance was evaluated with a Welch's *t* test.

Experiments were nonrandomized and nonblinded, and no prespecified sample size was estimated. Measurements were taken from distinct samples. All data are presented as means ± SEM, and all experiments were repeated from $N \geq 2$ different batches to mitigate biological variability. The number of experiments (n) as technical replicates is indicated in the figure legends. Significances are indicated in the figures using the following symbols: "*", $P < 0.05$; "**", $P < 0.01$; and "N.S.," not statistically different.

SUPPLEMENTARY MATERIALS

Supplementary material for this article is available at http://advances.sciencemag.org/cgi/content/full/6/44/eabc9174/DC1

View/request a protocol for this paper from *Bio-protocol*.

REFERENCES AND NOTES

1. P. Enyedi, G. Czirjak, Molecular background of leak K^+ currents: Two-pore domain potassium channels. *Physiol. Rev.* **90**, 559–605 (2010).
2. S. Feliciangeli, F. C. Chatelain, D. Bichet, F. Lesage, The family of K2P channels: Salient structural and functional properties. *J. Physiol.* **593** (Pt. 12), 2587–2603 (2015).
3. S. N. Bagriantsev, K. A. Clark, D. L. Minor Jr., Metabolic and thermal stimuli control K(2P)2.1 (TREK-1) through modular sensory and gating domains. *EMBO J.* **31**, 3297–3308 (2012).
4. S. N. Bagriantsev, R. Peyronnet, K. A. Clark, E. Honore, D. L. Minor Jr., Multiple modalities converge on a common gate to control K2P channel function. *EMBO J.* **30**, 3594–3606 (2011).
5. M. Schewe, E. Nematian-Ardestani, H. Sun, M. Musinszki, S. Cordeiro, G. Bucci, B. L. de Groot, S. J. Tucker, M. Rapedius, T. Baukrowitz, A non-canonical voltage-sensing mechanism controls gating in K2P K^+ channels. *Cell* **164**, 937–949 (2016).
6. P. L. Piechotta, M. Rapedius, P. J. Stansfeld, M. K. Bollepalli, G. Erhlich, I. Andres-Enguix, H. Fritzenschaft, N. Decher, M. S. P. Sansom, S. J. Tucker, T. Baukrowitz, The pore structure and gating mechanism of K2P channels. *EMBO J.* **30**, 3607–3619 (2011).
7. J. Lopez-Barneo, T. Hoshi, S. H. Heinemann, R. W. Aldrich, Effects of external cations and mutations in the pore region on C-type inactivation of Shaker potassium channels. *Receptors Channels* **1**, 61–71 (1993).
8. T. Baukrowitz, G. Yellen, Modulation of K^+ current by frequency and external [K^+]: A tale of two inactivation mechanisms. *Neuron* **15**, 951–960 (1995).
9. L. A. Pardo, S. H. Heinemann, H. Terlau, U. Ludewig, C. Lorra, O. Pongs, W. Stuhmer, Extracellular K^+ specifically modulates a rat brain K+ channel. *Proc. Natl. Acad. Sci. U.S.A.* **89**, 2466–2470 (1992).
10. A. Cohen, Y. Ben-Abu, S. Hen, N. Zilberberg, A novel mechanism for human K_{2P}2.1 channel gating. Facilitation of C-type gating by protonation of extracellular histidine residues. *J. Biol. Chem.* **283**, 19448–19455 (2008).
11. J. F. Cordero-Morales, L. G. Cuello, Y. Zhao, V. Jogini, D. M. Cortes, B. Roux, E. Perozo, Molecular determinants of gating at the potassium-channel selectivity filter. *Nat. Struct. Mol. Biol.* **13**, 311–318 (2006).
12. T. Hoshi, C. M. Armstrong, C-type inactivation of voltage-gated K^+ channels: Pore constriction or dilation? *J. Gen. Physiol.* **141**, 151–160 (2013).
13. Y. Zhou, R. MacKinnon, The occupancy of ions in the K^+ selectivity filter: Charge balance and coupling of ion binding to a protein conformational change underlie high conduction rates. *J. Mol. Biol.* **333**, 965–975 (2003).
14. Y. Zhou, J. H. Morais-Cabral, A. Kaufman, R. MacKinnon, Chemistry of ion coordination and hydration revealed by a K^+ channel-Fab complex at 2.0 Å resolution. *Nature* **414**, 43–48 (2001).
15. L. G. Cuello, D. M. Cortes, E. Perozo, The gating cycle of a K^+ channel at atomic resolution. *eLife* **6**, e28032 (2017).
16. L. G. Cuello, V. Jogini, D. M. Cortes, E. Perozo, Structural mechanism of C-type inactivation in K^+ channels. *Nature* **466**, 203–208 (2010).
17. V. Pau, Y. Zhou, Y. Ramu, Y. Xu, Z. Lu, Crystal structure of an inactivated mutant mammalian voltage-gated K^+ channel. *Nat. Struct. Mol. Biol.* **24**, 857–865 (2017).
18. W. Wang, R. MacKinnon, Cryo-EM structure of the open human ether-à-go-go-related K^+ Channel hERG. *Cell* **169**, 422–430.e10 (2017).

19. D. Matthies, C. Bae, G. E. S. Toombes, T. Fox, A. Bartesaghi, S. Subramaniam, K. J. Swartz, Single-particle cryo-EM structure of a voltage-activated potassium channel in lipid nanodiscs. *eLife* **7**, e37558 (2018).
20. M. Lolicato, C. Arrigoni, T. Mori, Y. Sekioka, C. Bryant, K. A. Clark, D. L. Minor Jr., K_{2P}2.1 (TREK-1)–activator complexes reveal a cryptic selectivity filter binding site. *Nature* **547**, 364–368 (2017).
21. Y. Y. Dong, A. C. W. Pike, A. Mackenzie, C. McClenaghan, P. Aryal, L. Dong, A. Quigley, M. Grieben, S. Goubin, S. Mukhopadhyay, G. F. Ruda, M. V. Clausen, L. Cao, P. E. Brennan, N. A. Burgess-Brown, M. S. P. Sansom, S. J. Tucker, E. P. Carpenter, K2P channel gating mechanisms revealed by structures of TREK-2 and a complex with Prozac. *Science* **347**, 1256–1259 (2015).
22. S. G. Brohawn, J. del Marmol, R. MacKinnon, Crystal structure of the human K2P TRAAK, a lipid- and mechano-sensitive K^+ ion channel. *Science* **335**, 436–441 (2012).
23. S. G. Brohawn, E. B. Campbell, R. MacKinnon, Domain-swapped chain connectivity and gated membrane access in a Fab-mediated crystal of the human TRAAK K^+ channel. *Proc. Natl. Acad. Sci. U.S.A.* **110**, 2129–2134 (2013).
24. S. G. Brohawn, E. B. Campbell, R. MacKinnon, Physical mechanism for gating and mechanosensitivity of the human TRAAK K^+ channel. *Nature* **516**, 126–130 (2014).
25. M. Lolicato, P. M. Riegelhaupt, C. Arrigoni, K. A. Clark, D. L. Minor Jr., Transmembrane helix straightening and buckling underlies activation of mechanosensitive and thermosensitive K(2P) channels. *Neuron* **84**, 1198–1212 (2014).
26. A. N. Miller, S. B. Long, Crystal structure of the human two-pore domain potassium channel K2P1. *Science* **335**, 432–436 (2012).
27. M. G. Derebe, D. B. Sauer, W. Zeng, A. Alam, N. Shi, Y. Jiang, Tuning the ion selectivity of tetrameric cation channels by changing the number of ion binding sites. *Proc. Natl. Acad. Sci. U.S.A.* **108**, 598–602 (2011).
28. D. Liebschner, P. V. Afonine, N. W. Moriarty, B. K. Poon, O. V. Sobolev, T. C. Terwilliger, P. D. Adams, Polder maps: Improving OMIT maps by excluding bulk solvent. *Acta Crystallogr. D Struct. Biol.* **73**, 148–157 (2017).
29. P. S. Langan, V. G. Vandavasi, K. L. Weiss, P. V. Afonine, K. el Omari, R. Duman, A. Wagner, L. Coates, Anomalous x-ray diffraction studies of ion transport in K^+ channels. *Nat. Commun.* **9**, 4540 (2018).
30. A. Wagner, R. Duman, K. Henderson, V. Mykhaylyk, In-vacuum long-wavelength macromolecular crystallography. *Acta Crystallogr. D Struct. Biol.* **72**, 430–439 (2016).
31. J. Ostmeyer, S. Chakrapani, A. C. Pan, E. Perozo, B. Roux, Recovery from slow inactivation in K^+ channels is controlled by water molecules. *Nature* **501**, 121–124 (2013).
32. A. Altis, P. H. Nguyen, R. Hegger, G. Stock, Dihedral angle principal component analysis of molecular dynamics simulations. *J. Chem. Phys.* **126**, 244111 (2007).
33. S. B. Long, X. Tao, E. B. Campbell, R. MacKinnon, Atomic structure of a voltage-dependent K^+ channel in a lipid membrane-like environment. *Nature* **450**, 376–382 (2007).
34. J. T. Brennecke, B. L. de Groot, Mechanism of mechanosensitive gating of the TREK-2 potassium channel. *Biophys. J.* **114**, 1336–1343 (2018).
35. M. P. Harrigan, K. A. McKiernan, V. Shanmugasundaram, R. A. Denny, V. S. Pande, Markov modeling reveals novel intracellular modulation of the human TREK-2 selectivity filter. *Sci. Rep.* **7**, 632 (2017).
36. N. Shi, S. Ye, A. Alam, L. Chen, Y. Jiang, Atomic structure of a Na^+- and K^+-conducting channel. *Nature* **440**, 570–574 (2006).
37. L. Pope, C. Arrigoni, H. Lou, C. Bryant, A. Gallardo-Godoy, A. R. Renslo, D. L. Minor Jr., Protein and chemical determinants of BL-1249 action and selectivity for K_{2P} channels. *ACS Chem. Neurosci.* **9**, 3153–3165 (2018).
38. M. Schewe, H. Sun, Ü. Mert, A. Mackenzie, A. C. W. Pike, F. Schulz, C. Constantin, K. S. Vowinkel, L. J. Conrad, A. K. Kiper, W. Gonzalez, M. Musinszki, M. Tegtmeier, D. C. Pryde, H. Belabed, M. Nazare, B. L. de Groot, N. Decher, B. Fakler, E. P. Carpenter, S. J. Tucker, T. Baukrowitz, A pharmacological master key mechanism that unlocks the selectivity filter gate in K^+ channels. *Science* **363**, 875–880 (2019).
39. N. Zilberberg, N. Ilan, S. A. N. Goldstein, KCNKØ. *Neuron* **32**, 635–648 (2001).
40. H. P. Larsson, F. Elinder, A conserved glutamate is important for slow inactivation in K^+ channels. *Neuron* **27**, 573–583 (2000).
41. P. Ortega-Sáenz, R. Pardal, A. Castellano, J. López-Barneo, Collapse of conductance is prevented by a glutamate residue conserved in voltage-dependent K^+ channels. *J. Gen. Physiol.* **116**, 181–190 (2000).
42. G. Sandoz, D. Douguet, F. Chatelain, M. Lazdunski, F. Lesage, Extracellular acidification exerts opposite actions on TREK1 and TREK2 potassium channels via a single conserved histidine residue. *Proc. Natl. Acad. Sci. U.S.A.* **106**, 14628–14633 (2009).
43. K. E. J. Rödström, A. K. Kiper, W. Zhang, S. Rinné, A. C. W. Pike, M. Goldstein, L. J. Conrad, M. Delbeck, M. G. Hahn, H. Meier, M. Platzk, A. Quigley, D. Speedman, L. Shrestha, S. M. M. Mukhopadhyay, N. A. Burgess-Brown, S. J. Tucker, T. Müller, N. Decher, E. P. Carpenter, A lower X-gate in TASK channels traps inhibitors within the vestibule. *Nature* **582**, 443–447 (2020).
44. S. A. Pless, J. D. Galpin, A. P. Niciforovic, H. T. Kurata, C. A. Ahern, Hydrogen bonds as molecular timers for slow inactivation in voltage-gated potassium channels. *eLife* **2**, e01289 (2013).
45. J. P. Lees-Miller, Y. Duan, G. Q. Teng, K. Thorstad, H. J. Duff, Novel gain-of-function mechanism in K^+ channel-related long-QT syndrome: Altered gating and selectivity in the HERG1 N629D mutant. *Circ. Res.* **86**, 507–513 (2000).
46. W. E. Miranda, K. R. DeMarco, J. Guo, H. J. Duff, I. Vorobyov, C. E. Clancy, S. Y. Noskov, Selectivity filter modalities and rapid inactivation of the hERG1 channel. *Proc. Natl. Acad. Sci. U.S.A.* **117**, 2795–2804 (2020).
47. D. Bockenhauer, N. Zilberberg, S. A. N. Goldstein, KCNK2: Reversible conversion of a hippocampal potassium leak into a voltage-dependent channel. *Nat. Neurosci.* **4**, 486–491 (2001).
48. M. V. Clausen, V. Jarerattanachat, E. P. Carpenter, M. S. P. Sansom, S. J. Tucker, Asymmetric mechanosensitivity in a eukaryotic ion channel. *Proc. Natl. Acad. Sci. U.S.A.* **114**, E8343–E8351 (2017).
49. M. Lengyel, G. Czirják, P. Enyedi, Formation of functional heterodimers by TREK-1 and TREK-2 two-pore domain potassium channel subunits. *J. Biol. Chem.* **291**, 13649–13661 (2016).
50. J. Levitz, P. Royal, Y. Comoglio, B. Wdziekonski, S. Schaub, D. M. Clemens, E. Y. Isacoff, G. Sandoz, Heterodimerization within the TREK channel subfamily produces a diverse family of highly regulated potassium channels. *Proc. Natl. Acad. Sci. U.S.A.* **113**, 4194–4199 (2016).
51. S. Blin, I. Ben Soussia, E.-J. Kim, F. Brau, D. Kang, F. Lesage, D. Bichet, Mixing and matching TREK/TRAAK subunits generate heterodimeric K_{2P} channels with unique properties. *Proc. Natl. Acad. Sci. U.S.A.* **113**, 4200–4205 (2016).
52. P. Royal, A. Andres-Bilbe, P. Á. Prado, C. Verkest, B. Wdziekonski, S. Schaub, A. Baron, F. Lesage, X. Gasull, J. Levitz, G. Sandoz, Migraine-associated TRESK mutations increase neuronal excitability through alternative translation initiation and inhibition of TREK. *Neuron* **101**, 232–245.e6 (2019).
53. S. Blin, F. C. Chatelain, S. Feliciangeli, D. Kang, F. Lesage, D. Bichet, Tandem pore domain halothane-inhibited K^+ channel subunits THIK1 and THIK2 assemble and form active channels. *J. Biol. Chem.* **289**, 28202–28212 (2014).
54. V. Renigunta, X. Zou, S. Kling, G. Schlichthörl, J. Daut, Breaking the silence: Functional expression of the two-pore-domain potassium channel THIK-2. *Pflugers Arch.* **466**, 1735–1745 (2014).
55. A. P. Berg, E. M. Talley, J. P. Manger, D. A. Bayliss, Motoneurons express heteromeric TWIK-related acid-sensitive K^+ (TASK) channels containing TASK-1 (KCNK3) and TASK-3 (KCNK9) subunits. *J. Neurosci.* **24**, 6693–6702 (2004).
56. A. Mathie, E. L. Veale, K. P. Cunningham, R. G. Holden, P. D. Wright, Two-pore domain potassium channels as drug targets: Anesthesia and beyond. *Annu. Rev. Pharmacol. Toxicol.* 10.1146/annurev-pharmtox-030920-111536 , (2020).
57. K. H. Yuill, P. J. Stansfeld, I. Ashmole, M. J. Sutcliffe, P. R. Stanfield, The selectivity, voltage-dependence and acid sensitivity of the tandem pore potassium channel TASK-1: Contributions of the pore domains. *Pflugers Arch.* **455**, 333–348 (2007).
58. S. Liu, P. J. Focke, K. Matulef, X. Bian, P. Moënne-Loccoz, F. I. Valiyaveetil, S. W. Lockless, Ion-binding properties of a K^+ channel selectivity filter in different conformations. *Proc. Natl. Acad. Sci. U.S.A.* **112**, 15096–15100 (2015).
59. J. Li, J. Ostmeyer, E. Boulanger, H. Rui, E. Perozo, B. Roux, Chemical substitutions in the selectivity filter of potassium channels do not rule out constricted-like conformations for C-type inactivation. *Proc. Natl. Acad. Sci. U.S.A.* **114**, 11145–11150 (2017).
60. J. Li, J. Ostmeyer, L. G. Cuello, E. Perozo, B. Roux, Rapid constriction of the selectivity filter underlies C-type inactivation in the KcsA potassium channel. *J. Gen. Physiol.* **150**, 1408–1420 (2018).
61. P. K. Devaraneni, A. G. Komarov, C. A. Costantino, J. J. Devereaux, K. Matulef, F. I. Valiyaveetil, Semisynthetic K^+ channels show that the constricted conformation of the selectivity filter is not the C-type inactivated state. *Proc. Natl. Acad. Sci. U.S.A.* **110**, 15698–15703 (2013).
62. E. A. W. van der Cruijsen, D. Nand, M. Weingarth, A. Prokofyev, S. Hornig, A. A. Cukkemane, A. M. J. J. Bonvin, S. Becker, R. E. Hulse, E. Perozo, O. Pongs, M. Baldus, Importance of lipid-pore loop interface for potassium channel structure and function. *Proc. Natl. Acad. Sci. U.S.A.* **110**, 13008–13013 (2013).
63. L. Ma, D. Roman-Campos, E. D. Austin, M. Eyries, K. S. Sampson, F. Soubrier, M. Germain, D.-A. Trégouët, A. Borczuk, E. B. Rosenzweig, B. Girerd, D. Montani, M. Humbert, J. E. Loyd, R. S. Kass, W. K. Chung, A novel channelopathy in pulmonary arterial hypertension. *N. Engl. J. Med.* **369**, 351–361 (2013).
64. S. Jekhmane, J. Medeiros-Silva, J. Li, F. Kümmerer, C. Müller-Hermes, M. Baldus, B. Roux, M. Weingarth, Shifts in the selectivity filter dynamics cause modal gating in K^+ channels. *Nat. Commun.* **10**, 123 (2019).
65. F. Maingret, I. Lauritzen, A. J. Patel, C. Heurteaux, R. Reyes, F. Lesage, M. Lazdunski, E. Honoré, TREK-1 is a heat-activated background K^+ channel. *EMBO J.* **19**, 2483–2491 (2000).
66. A. J. Patel, E. Honoré, F. Maingret, F. Lesage, M. Fink, F. Duprat, M. Lazdunski, A mammalian two pore domain mechano-gated S-like K^+ channel. *EMBO J.* **17**, 4283–4290 (1998).

67. J. Chemin, A. J. Patel, F. Duprat, I. Lauritzen, M. Lazdunski, E. Honoré, A phospholipid sensor controls mechanogating of the K^+ channel TREK-1. *EMBO J.* **24**, 44–53 (2004).
68. E. Honoré, F. Maingret, M. Lazdunski, A. J. Patel, An intracellular proton sensor commands lipid- and mechano-gating of the K^+ channel TREK-1. *EMBO J.* **21**, 2968–2976 (2002).
69. Y. Kim, H. Bang, C. Gnatenco, D. Kim, Synergistic interaction and the role of C-terminus in the activation of TRAAK K^+ channels by pressure, free fatty acids and alkali. *Pflugers Arch.* **442**, 64–72 (2001).
70. Y. Kim, C. Gnatenco, H. Bang, D. Kim, Localization of TREK-2 K^+ channel domains that regulate channel kinetics and sensitivity to pressure, fatty acids and pH_i. *Pflugers Arch.* **442**, 952–960 (2001).
71. C. McClenaghan, M. Schewe, P. Aryal, E. P. Carpenter, T. Baukrowitz, S. J. Tucker, Polymodal activation of the TREK-2 K2P channel produces structurally distinct open states. *J. Gen. Physiol.* **147**, 497–505 (2016).
72. C. Heurteaux, N. Guy, C. Laigle, N. Blondeau, F. Duprat, M. Mazzuca, L. Lang-Lazdunski, C. Widmann, M. Zanzouri, G. Romey, M. Lazdunski, TREK-1, a K^+ channel involved in neuroprotection and general anesthesia. *EMBO J.* **23**, 2684–2695 (2004).
73. R. M. Lazarenko, M. G. Fortuna, Y. Shi, D. K. Mulkey, A. C. Takakura, T. S. Moreira, P. G. Guyenet, D. A. Bayliss, Anesthetic activation of central respiratory chemoreceptor neurons involves inhibition of a THIK-1-like background K^+ current. *J. Neurosci.* **30**, 9324–9334 (2010).
74. A. Alloui, K. Zimmermann, J. Mamet, F. Duprat, J. Noël, J. Chemin, N. Guy, N. Blondeau, N. Voilley, C. Rubat-Coudert, M. Borsotto, G. Romey, C. Heurteaux, P. Reeh, A. Eschalier, M. Lazdunski, TREK-1, a K^+ channel involved in polymodal pain perception. *EMBO J.* **25**, 2368–2376 (2006).
75. M. Devilliers, J. Busserolles, S. Lolignier, E. Deval, V. Pereira, A. Alloui, M. Christin, B. Mazet, P. Delmas, J. Noel, M. Lazdunski, A. Eschalier, Activation of TREK-1 by morphine results in analgesia without adverse side effects. *Nat. Commun.* **4**, 2941 (2013).
76. D. Vivier, I. B. Soussia, N. Rodrigues, S. Lolignier, M. Devilliers, F. C. Chatelain, L. Prival, E. Chapuy, G. Bourdier, K. Bennis, F. Lesage, A. Eschalier, J. Busserolles, S. Ducki, Development of the first two-pore domain potassium channel TWIK-related K^+ channel 1-selective agonist possessing in vivo antinociceptive activity. *J. Med. Chem.* **60**, 1076–1088 (2017).
77. N. Decher, B. Ortiz-Bonnin, C. Friedrich, M. Schewe, A. K. Kiper, S. Rinné, G. Seemann, R. Peyronnet, S. Zumhagen, D. Bustos, J. Kockskämper, P. Kohl, S. Just, W. González, T. Baukrowitz, B. Stallmeyer, E. Schulze-Bahr, Sodium permeable and "hypersensitive" TREK-1 channels cause ventricular tachycardia. *EMBO Mol. Med.* **9**, 403–414 (2017).
78. X. Wu, Y. Liu, X. Chen, Q. Sun, R. Tang, W. Wang, Z. Yu, M. Xie, Involvement of TREK-1 activity in astrocyte function and neuroprotection under simulated ischemia conditions. *J. Mol. Neurosci.* **49**, 499–506 (2013).
79. W. Kabsch, Xds. *Acta Crystallogr. D Biol. Crystallogr.* **66**, 125–132 (2010).
80. P. R. Evans, G. N. Murshudov, How good are my data and what is the resolution? *Acta Crystallogr. D Biol. Crystallogr.* **69**, 1204–1214 (2013).
81. P. A. Karplus, K. Diederichs, Assessing and maximizing data quality in macromolecular crystallography. *Curr. Opin. Struct. Biol.* **34**, 60–68 (2015).
82. P. Emsley, K. Cowtan, Coot: Model-building tools for molecular graphics. *Acta Crystallogr. D Biol. Crystallogr.* **60**, 2126–2132 (2004).
83. Collaborative Computational Project, Number 4, The CCP4 suite: Programs for protein crystallography. *Acta Crystallogr. D Biol. Crystallogr.* **50**, 760–763 (1994).
84. P. D. Adams, P. V. Afonine, G. Bunkóczi, V. B. Chen, I. W. Davis, N. Echols, J. J. Headd, L.-W. Hung, G. J. Kapral, R. W. Grosse-Kunstleve, A. J. McCoy, N. W. Moriarty, R. Oeffner, R. J. Read, D. C. Richardson, J. S. Richardson, T. C. Terwilliger, P. H. Zwart, PHENIX: A comprehensive Python-based system for macromolecular structure solution. *Acta Crystallogr. D Biol. Crystallogr.* **66**, 213–221 (2010).
85. O. S. Smart, T. O. Womack, C. Flensburg, P. Keller, W. Paciorek, A. Sharff, C. Vonrhein, G. Bricogne, Exploiting structure similarity in refinement: Automated NCS and target-structure restraints in BUSTER. *Acta Crystallogr. D Biol. Crystallogr.* **68**, 368–380 (2012).
86. A. Thorn, G. M. Sheldrick, ANODE: Anomalous and heavy-atom density calculation. *J. Appl. Cryst.* **44**, 1285–1287 (2011).
87. P. S. Huang, Y.-E. A. Ban, F. Richter, I. Andre, R. Vernon, W. R. Schief, D. Baker, RosettaRemodel: A generalized framework for flexible backbone protein design. *PLOS ONE* **6**, e24109 (2011).
88. S. Jo, T. Kim, W. Im, Automated builder and database of protein/membrane complexes for molecular dynamics simulations. *PLOS ONE* **2**, e880 (2007).
89. J. Huang, S. Rauscher, G. Nawrocki, T. Ran, M. Feig, B. L. de Groot, H. Grubmüller, A. D. MacKerell Jr., CHARMM36m: An improved force field for folded and intrinsically disordered proteins. *Nat. Methods* **14**, 71–73 (2017).
90. J. B. Klauda, R. M. Venable, J. A. Freites, J. W. O'Connor, D. J. Tobias, C. Mondragon-Ramirez, I. Vorobyov, A. D. MacKerell Jr., R. W. Pastor, Update of the CHARMM all-atom additive force field for lipids: Validation on six lipid types. *J. Phys. Chem. B* **114**, 7830–7843 (2010).
91. W. L. Jorgensen, J. Chandrasekhar, J. D. Madura, R. W. Impey, M. L. Klein, Comparison of simple potential functions for simulating liquid water. *J. Chem. Phys.* **79**, 926–935 (1983).
92. K. Vanommeslaeghe, E. Hatcher, C. Acharya, S. Kundu, S. Zhong, J. Shim, E. Darian, O. Guvench, P. Lopes, I. Vorobyov, A. D. Mackerell Jr., CHARMM general force field: A force field for drug-like molecules compatible with the CHARMM all-atom additive biological force fields. *J. Comput. Chem.* **31**, 671–690 (2010).
93. K. Vanommeslaeghe, A. D. MacKerell Jr., Automation of the CHARMM General Force Field (CGenFF) I: Bond perception and atom typing. *J. Chem. Inf. Model.* **52**, 3144–3154 (2012).
94. K. Vanommeslaeghe, E. P. Raman, A. D. MacKerell Jr., Automation of the CHARMM General Force Field (CGenFF) II: Assignment of bonded parameters and partial atomic charges. *J. Chem. Inf. Model.* **52**, 3155–3168 (2012).
95. D. Beglov, B. Roux, Finite representation of an infinite bulk system: Solvent boundary potential for computer simulations. *J. Chem. Phys.* **100**, 9050–9063 (1994).
96. D. E. Shaw, J. P. Grossman, J. A. Bank, B. Batson, J. A. Butts, J. C. Chao, M. M. Deneroff, R. O. Dror, A. Even, C. H. Fenton, A. Forte, J. Gagliardo, G. Gill, B. Greskamp, C. R. Ho, D. J. Ierardi, L. Iserovich, J. S. Kuskin, R. H. Larson, T. Layman, L.-S. Lee, A. K. Lerer, C. Li, D. Killebrew, K. M. Mackenzie, S. Y.-H. Mok, M. A. Moraes, R. Mueller, L. J. Nociolo, J. L. Peticolas, T. Quan, D. Ramot, J. K. Salmon, D. P. Scarpazza, U. B. Schafer, N. Siddique, C. W. Snyder, J. Spengler, P. T. P. Tang, M. Theobald, H. Toma, B. Towles, B. Vitale, S. C. Wang, C. Young, Anton 2: Raising the bar for performance and programmability in a special-purpose molecular dynamics supercomputer, in *Proceedings of the International Conference for High Performance Computing, Networking, Storage and Analysis* (*SC '14*) (IEEE, 2014), pp. 41–53.
97. M. J. Abraham, T. Murtola, R. Schulz, S. Páll, J. C. Smith, B. Hess, E. Lindahl, GROMACS: High performance molecular simulations through multi-level parallelism from laptops to supercomputers. *SoftwareX* **1-2**, 19–25 (2015).
98. J. Gumbart, F. Khalili-Araghi, M. Sotomayor, B. Roux, Constant electric field simulations of the membrane potential illustrated with simple systems. *Biochim. Biophys. Acta* **1818**, 294–302 (2012).
99. J. C. Phillips, R. Braun, W. Wang, J. Gumbart, E. Tajkhorshid, E. Villa, C. Chipot, R. D. Skeel, L. Kalé, K. Schulten, Scalable molecular dynamics with NAMD. *J. Comput. Chem.* **26**, 1781–1802 (2005).
100. G. J. Martyna, D. J. Tobias, M. L. Klein, Constant-pressure molecular-dynamics algorithms. *J. Chem. Phys.* **101**, 4177–4189 (1994).
101. S. Nosé, A molecular dynamics method for simulations in the canonical ensemble. *Mol. Phys.* **52**, 255–268 (1984).
102. W. G. Hoover, Canonical dynamics: Equilibrium phase-space distributions. *Phys. Rev. A* **31**, 1695–1697 (1985).
103. Y. Shan, J. L. Klepeis, M. P. Eastwood, R. O. Dror, D. E. Shaw, Gaussian split Ewald: A fast Ewald mesh method for molecular simulation. *J. Chem. Phys.* **122**, 054101 (2005).
104. J.-P. Ryckaert, G. Ciccotti, H. J. C. Berendsen, Numerical integration of the cartesian equations of motion of a system with constraints: Molecular dynamics of *n*-alkanes. *J. Comput. Phys.* **23**, 327–341 (1977).
105. M. Parrinello, A. Rahman, Polymorphic transitions in single-crystals: A new molecular-dynamics method. *J. Appl. Phys.* **52**, 7182–7190 (1981).
106. S. Nosé, M. L. Klein, Constant pressure molecular-dynamics for molecular systems. *Mol. Phys.* **50**, 1055–1076 (2006).
107. T. Darden, D. York, L. Pedersen, Particle mesh Ewald: An N·log(N) method for Ewald sums in large systems. *J. Chem. Phys.* **98**, 10089–10092 (1993).
108. B. Hess, H. Bekker, H. J. C. Berendsen, J. G. E. M. Fraaije, LINCS: A linear constraint solver for molecular simulations. *J. Comput. Chem.* **18**, 1463–1472 (1997).
109. N. Michaud-Agrawal, E. J. Denning, T. B. Woolf, O. Beckstein, MDAnalysis: A toolkit for the analysis of molecular dynamics simulations. *J. Comput. Chem.* **32**, 2319–2327 (2011).
110. H. Guizouarn, N. Gabillat, R. Motais, F. Borgese, Multiple transport functions of a red blood cell anion exchanger, tAE1: Its role in cell volume regulation. *J. Physiol.* **535**, 497–506 (2001).

Acknowledgments: We thank C. Arrigoni and L. Pope for electrophysiology guidance, C. Colleran for cell culture assistance, B. Roux for guidance on our choice of force fields used in this study, L. Jan for support, and K. Brejc and F. C. Chatelain for comments on the manuscript. **Funding:** This work was supported by NIH grants R21NS091941 to J.M.R., R01GM089740 to M.G., and R01-MH093603 to D.L.M. and an AHA postdoctoral fellowship to F.A.-A. Anton 2 computer time was provided by the Pittsburgh Supercomputing Center (PSC) through NIH grant R01GM116961. The Anton 2 machine at PSC was made available by D.E. Shaw Research. Simulations were also carried out on the UCSF Wynton Cluster made possible through NIH grant 1S10OD021596. **Author contributions:** M.L., A.M.N., F.A.-A., S.C., J.M.R., M.G., and D.L.M. conceived the study and designed the experiments. M.L. expressed, purified,

and crystallized the proteins, collected diffraction data, and determined the structures. R.D. and A.W. collected anomalous diffraction data. M.L., A.M.N., F.A.-A., and, D.C. performed functional studies. F.A.-A. carried out and analyzed single-channel recordings. A.M.N., S.C., J.M.R., and M.G. designed and executed the simulations. M.L., A.M.N., F.A.-A., D.C., M.G., and D.L.M. analyzed the data. M.G. and D.L.M. provided guidance and support. M.L., A.M.N., F.A.-A., M.G., and D.L.M. wrote the paper. **Competing interests:** The authors declare that they have no competing interests. **Materials and correspondence:** Correspondence should be directed to M.G. or D.L.M. Requests for materials should be directed to D.L.M. **Data and materials availability:** All data needed to evaluate the conclusions in the paper are present in the paper and/or the Supplementary Materials. Coordinates and structures factors are deposited in the RCSB and will be released immediately upon publication. Additional data related to this paper may be requested from the authors.

Submitted 20 May 2020
Accepted 10 September 2020
Published 30 October 2020
10.1126/sciadv.abc9174

Citation: M. Lolicato, A. M. Natale, F. Abderemane-Ali, D. Crottès, S. Capponi, R. Duman, A. Wagner, J. M. Rosenberg, M. Grabe, D. L. Minor Jr., K_{2P} channel C-type gating involves asymmetric selectivity filter order-disorder transitions. *Sci. Adv.* **6**, eabc9174 (2020).

Science Advances

K_{2P} channel C-type gating involves asymmetric selectivity filter order-disorder transitions

Marco Lolicato, Andrew M. Natale, Fayal Abderemane-Ali, David Crottès, Sara Capponi, Ramona Duman, Armin Wagner, John M. Rosenberg, Michael Grabe and Daniel L. Minor, Jr.

Sci Adv **6** (44), eabc9174.
DOI: 10.1126/sciadv.abc9174

Science Advances
AAAS

advances.sciencemag.org/cgi/content/full/6/44/eabc9174/DC1

Supplementary Materials for

K_{2P} channel C-type gating involves asymmetric selectivity filter order-disorder transitions

Marco Lolicato, Andrew M. Natale, Fayal Abderemane-Ali, David Crottès, Sara Capponi, Ramona Duman, Armin Wagner, John M. Rosenberg, Michael Grabe*, Daniel L. Minor Jr.*

*Corresponding author. Email: michael.grabe@ucsf.edu (M.G.); daniel.minor@ucsf.edu (D.L.M)

Published 30 October 2020, *Sci. Adv.* **6**, eabc9174 (2020)
DOI: 10.1126/sciadv.abc9174

The PDF file includes:

Other Supplementary Material for this manuscript includes the following:

(available at advances.sciencemag.org/cgi/content/full/6/44/eabc9174/DC1)

a

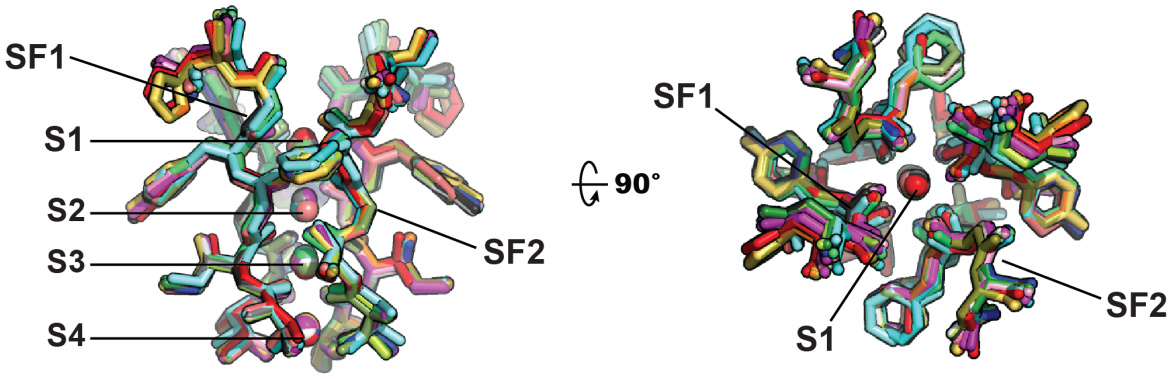

b

Structure (M4 status)	PDB code	Ion concentration	RMSD$_{C\alpha}$(Å)
K_{2P}2.1 (TREK-1) (up)	6CQ6	200 mM KCl	N.A.
K_{2P}2.1 (TREK-1):ML335(up)	6CQ8	200 mM KCl	0.25
K_{2P}2.1 (TREK-1):ML402 (up)	6CQ9	200 mM KCl	0.33
K_{2P}10.1 (TREK-2) (up)	4BW5	200 mM KCl	0.30/0.31
K_{2P}10.1 (TREK-2) (down)	4XDJ	200 mM KCl	0.33/0.33
K_{2P}10.1 (TREK-2):norfluoxitine (down)	4XDK	200 mM KCl	0.32/0.27
K_{2P}4.1 (TRAAK) (down)	3UM7	150 mM KCl*	0.55
K_{2P}4.1 (TRAAK):Fab (down)	4I9W	150 mM KCl*	0.38
K_{2P}4.1 (TRAAK):Fab (up)	4WFE	150 mM KCl*	0.38
K_{2P}4.1 (TRAAK):Fab (down)	4WFF	150 mM KCl*	0.37
K_{2P}4.1 (TRAAK):Fab (up)	4WFG	150 mM $TlNO_3$*	0.37
K_{2P}4.1 (TRAAK):Fab (up)	4WFH	150 mM $TlNO_3$*	0.39
K_{2P}4.1 (TRAAK) G124I (down)	4RUE	150 mM KCl*	0.36
K_{2P}4.1 (TRAAK) W262S (down)	4RUF	150 mM KCl*	0.38
K_{2P}1.1 (TWIK-1) (down)	3UKM	150 mM KCl	0.41/0.42
K_{2P}3.1 (TASK-1) (X-gate, down)	6RV2	200 mM KCl	0.33/0.34
K_{2P}3.1 (TASK-1) (X-gate, down)	6RV3	200 mM KCl	0.33/0.34
K_{2P}3.1 (TASK-1) (X-gate, down)	6RV4	200 mM KCl	0.34/0.35

Fig. S1 K_{2P} channel selectivity filters structure comparison. a, Superposition of the selectivity filters and permeant ions for: K_{2P}2.1 (TREK-1) (6CQ6)(*20*) (smudge), K_{2P}2.1 (TREK-1):ML335 (6CQ8)(*20*) (deep salmon), K_{2P}2.1 (TREK-1):ML402 (cyan) (6CQ9)(*20*); K_{2P}10.1 (TREK-2) (4BW5)(*21*) (pink), (4XDJ)(*21*) (magenta), (4XDK)(*21*) (purple); K_{2P}4.1 (TRAAK) (3UM7)(*22*) (aquamarine), (4I9W)(*23*) (limon), (4WFE) (forest green)(*24*), (4WFF) (white)(*24*),(4WFG) (grey)(*24*), (4WFH) (black)(*24*); K_{2P}4.1 (TRAAK) G124I (4RUE) (blue)(*25*) K_{2P}4.1 (TRAAK) W262S (4RUF) (lime green)(*25*); K_{2P}1.1 (TWIK-1) (3UKM)(*26*) (red). K_{2P}3.1 (TASK-1) (6RV2) (orange)(*43*), K_{2P}3.1 (TASK-1):BAY1000493 (6RV3) (yellow orange)(*43*), and K_{2P}3.1 (TASK-1):BAY2341237(6RV4) (olive)(*43*). SF1, SF2 and ion binding positions, S1-S4, are indicated. Ions are shown as spheres and colored according to the parent structure. **b,** K_{2P} channel structures, permeant ion concentration in crystallization conditions, and RMSD for all selectivity filter backbone atoms relative to K_{2P}2.1 (TREK-1) (6CQ6)(*20*). Structures with two RMSD values indicate

structures having chains A/B and C/D, respectively. '*' indicates samples where permeant ions were part of the protein sample buffer.

Fig. S2

Lolicato *et al.*

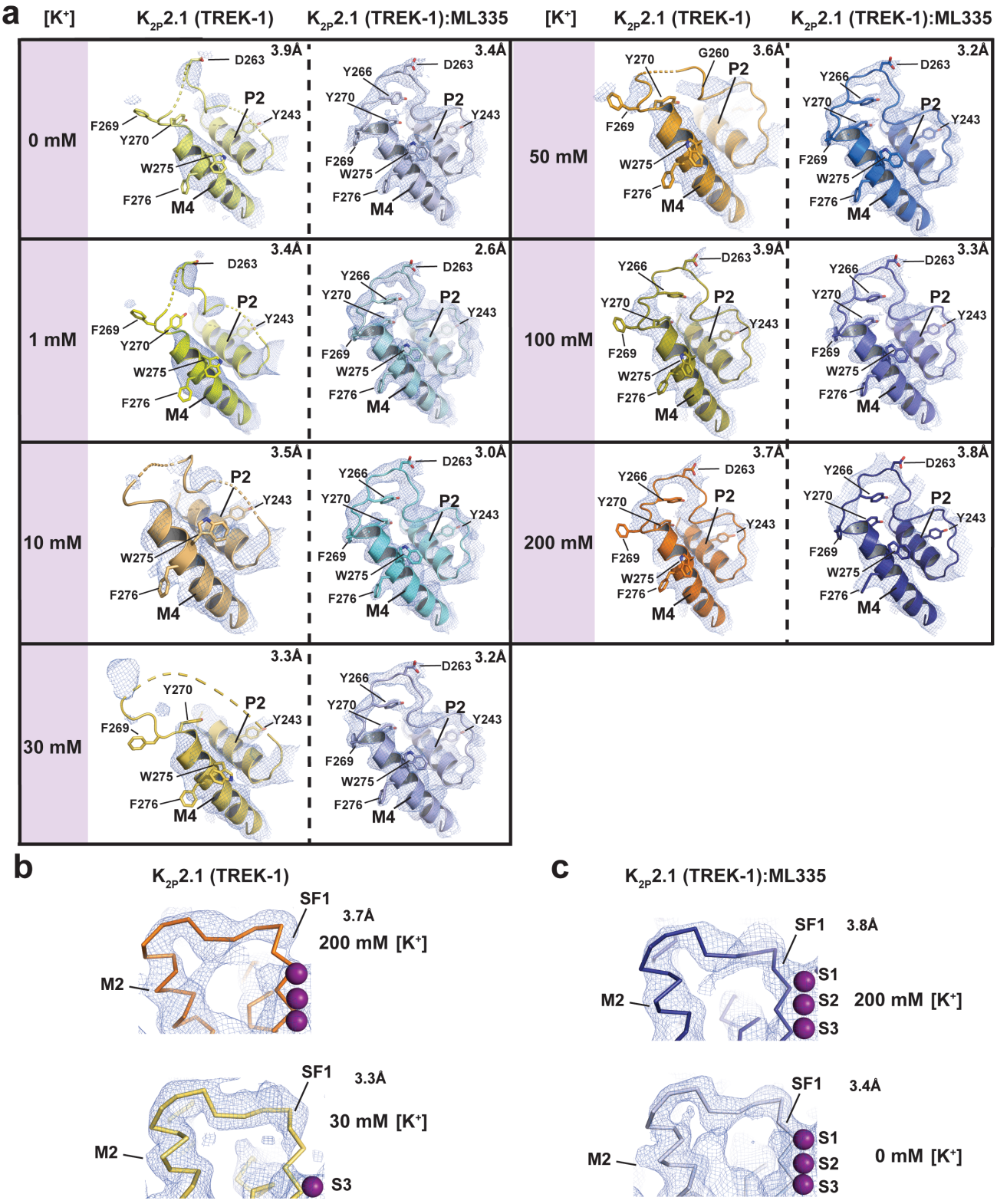

Fig. S2 K_{2P}2.1 (TREK-1) selectivity filter potassium-dependent conformational changes. a, SF2 exemplar 2Fo-Fc electron density (1σ) for K_{2P}2.1 (TREK-1) (left) and K_{2P}2.1 (TREK-1):ML335 (right) structures under 0 mM (pale yellow; blue white), 1 mM (yellow; pale cyan), 10 mM (light orange;

aquamarine) , 30 mM (yellow orange; light blue), 50 mM (bright orange; marine), 100 mM (olive; slate), and 200 mM (orange; deep blue) [K^+]. Dashed lines indicate regions of disorder. Resolution and select residues and channel elements are indicated. **b,** and **c** Exemplar SF1-M2 loop density for **b,** $K_{2P}2.1$ (TREK-1) under 30 mM (yellow orange) and 200 mM (orange) [K^+] and c, $K_{2P}2.1$ (TREK-1):ML335 under 0 mM (blue white) and 200 mM (deep blue) [K^+]. Examples show that the highest resolution low [K^+] structure, 30 mM [K^+], has a well-defined SF1-M2 loop, contrasting the poorly resolved SF2-M4 loop. Hence, the structural changes are local and not related to resolution.

Fig. S3

Lolicato *et al.*

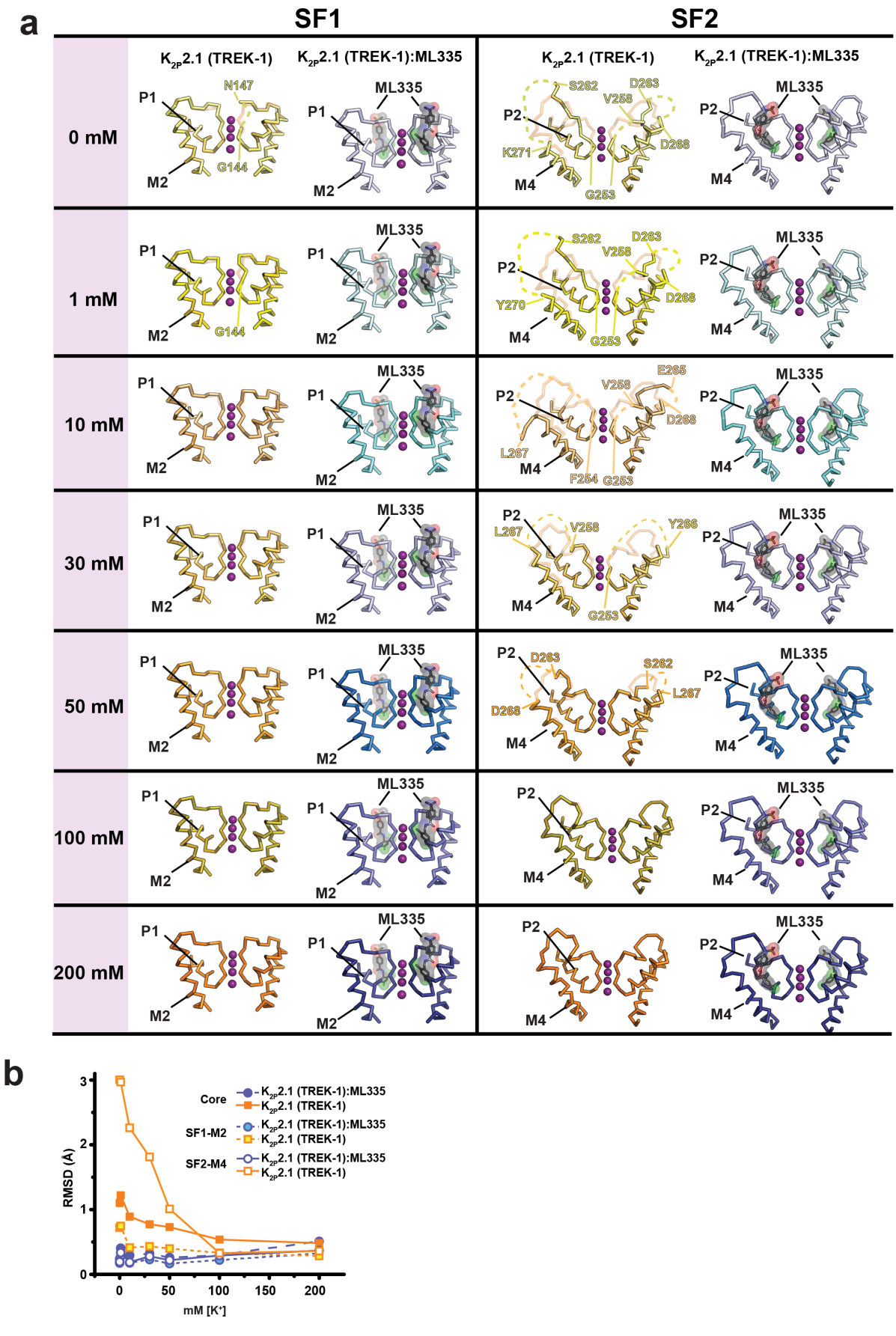

Fig. S3 Selectivity filter structural changes as a function of potassium concentration. a, $K_{2P}2.1$ (TREK-1) and the $K_{2P}2.1$ (TREK-1):ML335 complex SF1 and SF2 structures determined at the indicated potassium concentrations: 0 mM (pale yellow; blue white), 1 mM (yellow; pale cyan), 10 mM (light orange; aquamarine) , 30 mM (yellow orange; light blue), 50 mM (bright orange; marine), 100 mM (olive; slate), and 200 mM [K^+] (orange; deep blue). $K_{2P}2.1$ (TREK-1) panels show an overlay with the 200 mM [K^+] $K_{2P}2.1$ (TREK-1) structure in lighter shading. Labels indicate the last visible residue at points where the chain becomes disordered. Potassium ions from the 200 mM [K^+] structures are shown in all panels as a reference. **b,** $K_{2P}2.1$ (TREK-1) and $K_{2P}2.1$ (TREK-1):ML335 complex $RMSD_{C\alpha}$ as a function of [K^+]. Structures are compared to $K_{2P}2.1$ (TREK-1) in 200 mM [K^+] (PDB:6CQ6) and $K_{2P}2.1$ (TREK-1):ML335 complex in 200 mM [K^+] (PDB:6CQ8), respectively. Channel elements are grouped as follows: Core: residues 50-146, 153-255, 269-311; SF1-M2: residues 142-188; and SF2-M4: residues 251-295.

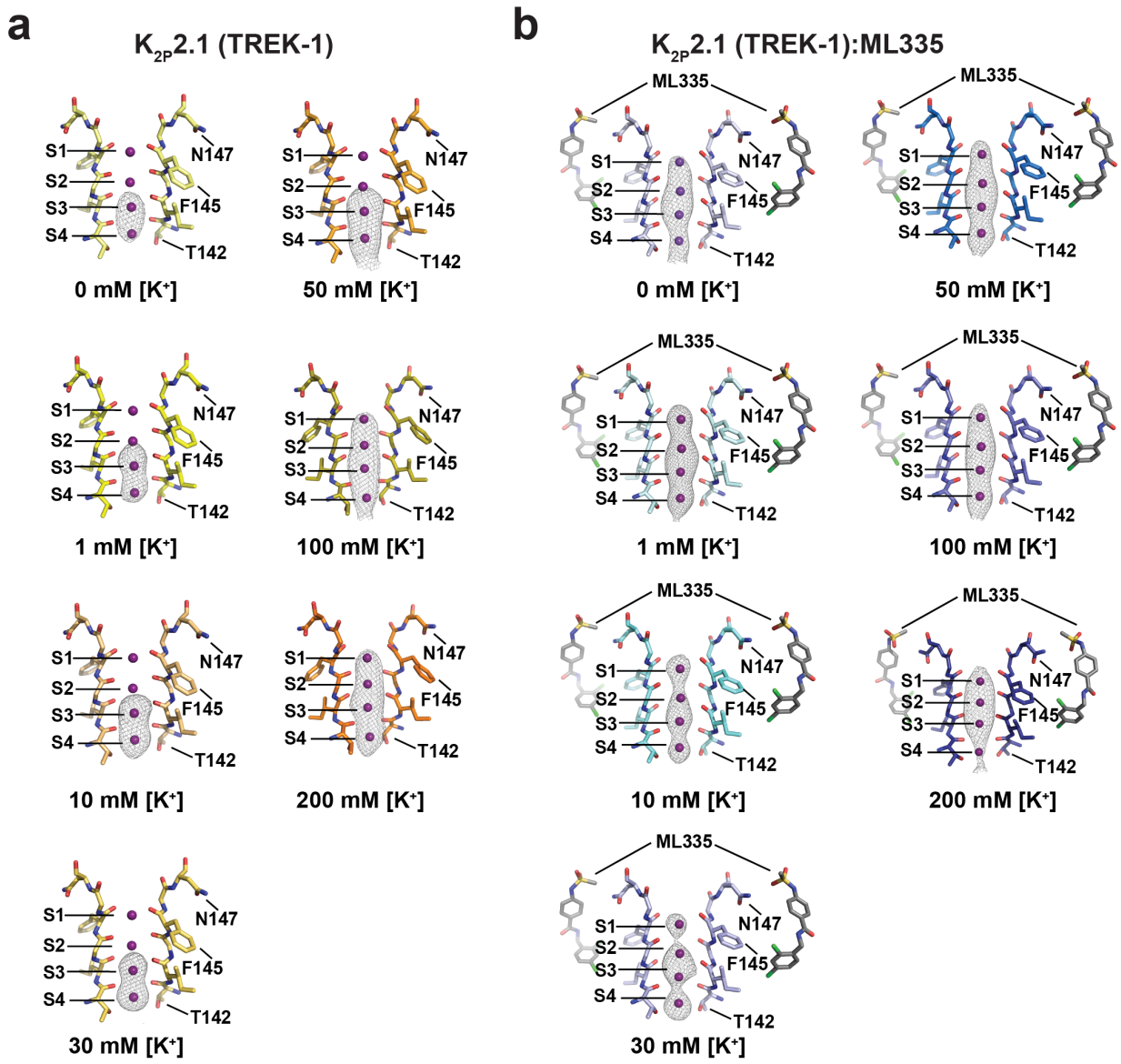

Fig. S4 Omit maps showing K_{2P}2.1 (TREK-1) selectivity filter ion occupancy as a function of [K+]. **a,b,** Polder omit maps(*28*) for structures of K_{2P}2.1 (TREK-1) determined in 0 mM [K+] (pale yellow) (5σ), 1 mM [K+] (yellow) (4σ), 10 mM [K+] (light orange) (5σ), 30 mM [K+] (yellow orange) (4σ), 50 mM [K+] (bright orange)(5σ), 100 mM [K+] (olive) (4σ), and 200 mM [K+] (orange)(4σ) (**a**) or K_{2P}2.1 (TREK-1):ML335 determined in 0 mM [K+] (blue white) (4σ), 1 mM [K+] (pale cyan) (4σ), 10 mM [K+] (aquamarine) (4σ), 30 mM [K+] (light blue) (4σ), 50 mM [K+] (marine) (4σ), 100 mM [K+] (slate) (4σ) and 200 mM [K+] (deep blue) (4σ) (**b**). Potassium ions are magenta spheres. Sites S1-S4 are labeled. ML335 is shown as sticks. SF1 in the 200 mM [K+] conformation is shown for all panels. Select residues are indicated.

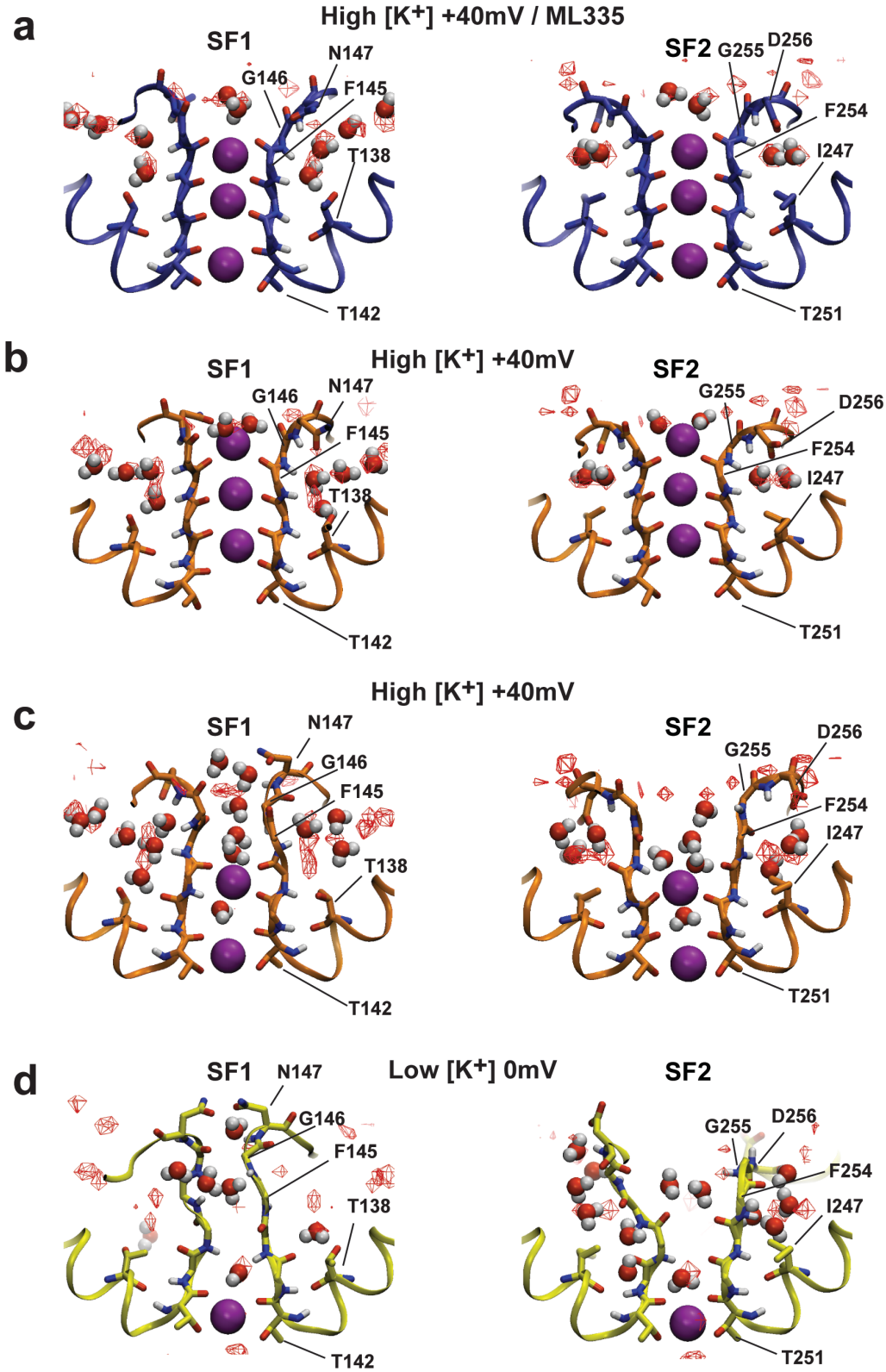

Fig. S5 Water interactions with the selectivity filter. a, Final frame of High [K+]/ +40 mV/ML335 simulation 4, showing SF1 (left) and SF2 (right). **b,** Final frame of High [K+]/+40 mV simulation 12. **c,** Final frame of High [K+]/+40 mV simulation 21. **d**, Final frame of Low [K+]/0 mV simulation 29. In all panels, water molecules interacting with the extracellular face of the selectivity filter are shown as spheres. Water oxygen

atom occupancy maps calculated from the simulation data are shown as red mesh and are contoured at the same level (density contains voxels with occupancy >7%) in all panels. Maps in **a** and **d** were calculated from all High [K^+]/+40 mV/ML335 and Low [K^+]/0 mV simulation trajectories, respectively. Map in **b** and **c** was calculated from all High [K^+]/+40 mV simulation trajectories. **c** and **d** show examples where filters have become disordered.

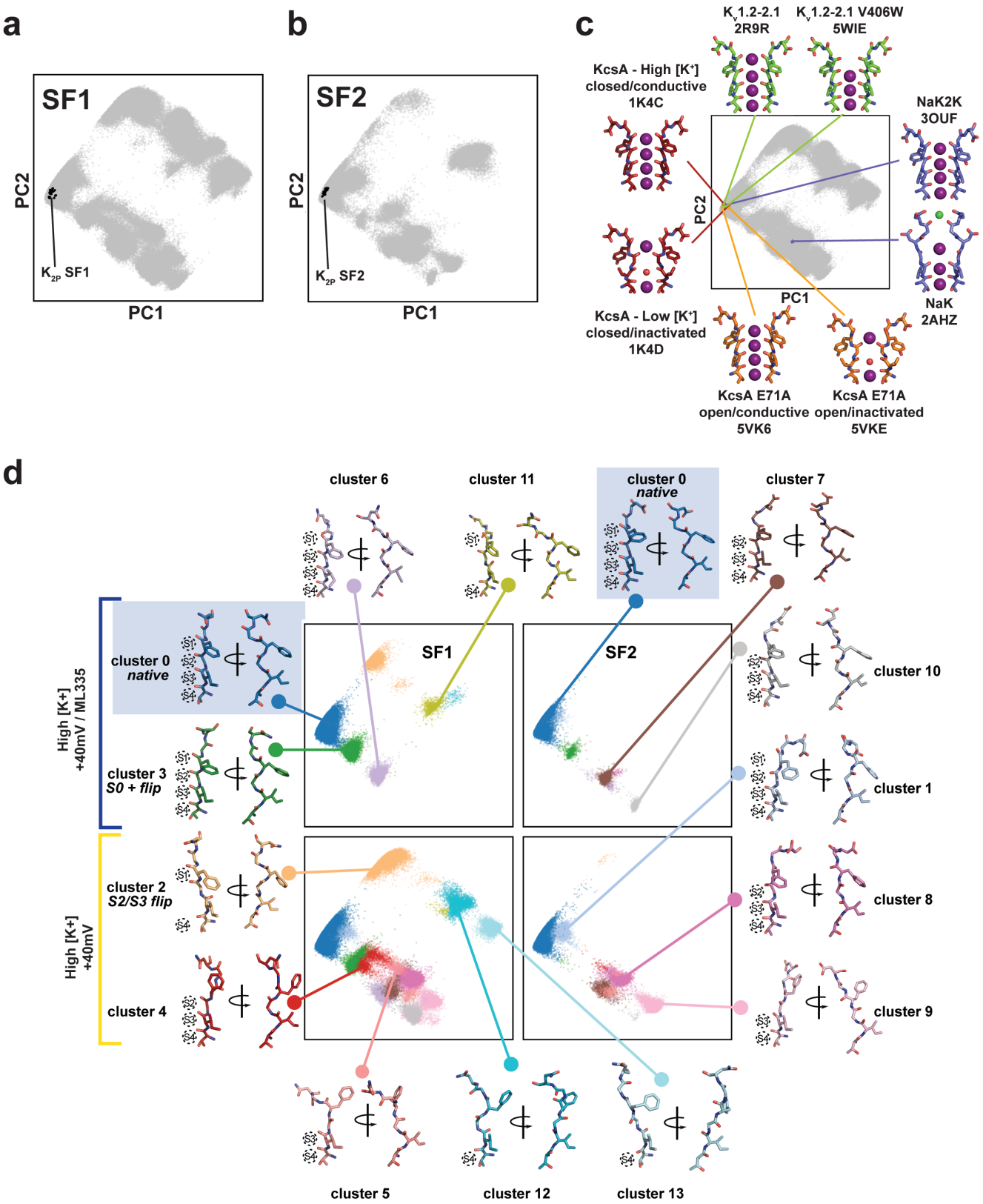

Fig. S6 K_{2P}2.1 (TREK-1) principal component analysis (PCA). a,b, PCA projection of selectivity filter conformations for SF1 (**a**) and SF2 (**b**). Grey points indicate K_{2P}2.1 (TREK-1) conformations from all simulations in this work; black points represent projections of SF1 and SF2 conformations obtained from

the Fig. S1b K_{2P} crystal structures. **c**, Representative non-K_{2P} selectivity filter conformations and their projections into PCA space. Grey points indicate K_{2P}2.1 (TREK-1) conformations from all simulations (SF1 and SF2). Lines and colored points show the PCA projected location of SF conformations from the indicated tetrameric potassium channel crystal structures: KcsA closed/conductive (1K4C) and closed/inactivated (1K4D)(*14*) (firebrick); Kv1.2-2.1 chimera (2R9R)(*33*) and V406W mutant (5WIE)(*17*) (chartreuse); NaK (2AHZ)(*36*) and K^+ selective mutant NaK2K (3OUF)(*27*) (slate); and KcsA E71A open/conductive (5VK6) and open/inactivated (5VKE)(*15*) (orange). **d**, Hierarchical clustering of SF conformations from all High [K^+] simulations. Clustering was performed on PC1-3, for clarity only PC1 and PC2 are shown. Points representing selectivity filter conformations in PCA space are colored according to their membership in one of 14 identified clusters. A single representative conformation is shown for each cluster, with the exception of the native state (cluster 0) for which representative conformations from both SF1 and SF2 are shown. For each representative conformation intact ion binding sites are indicated with dotted circles.

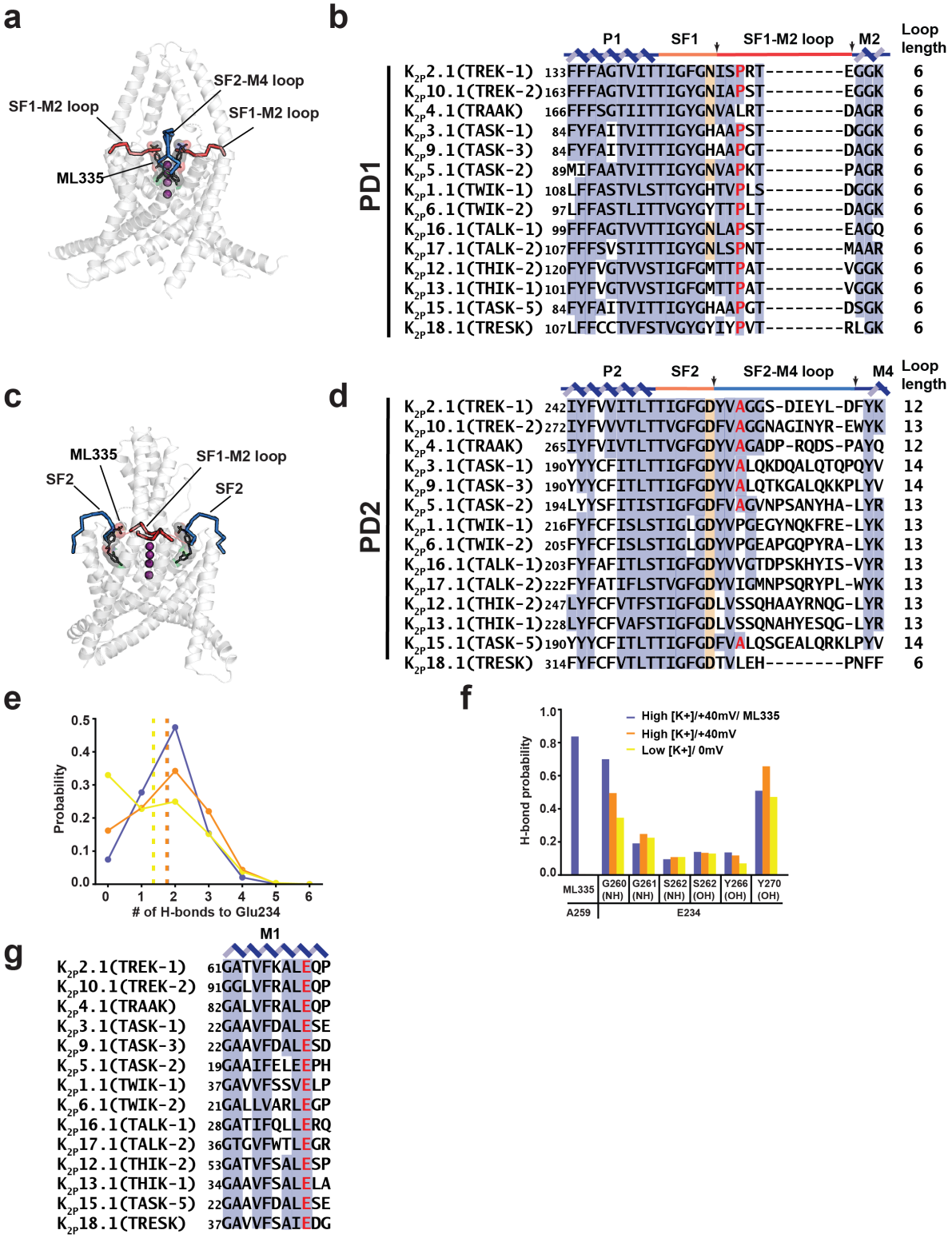

Fig. S7 K_{2P} channel pore domain comparisons. a, K_{2P}2.1 (TREK-1):ML335 complex (white) with a view showing the SF1-M2 loop. SF1-M2 loop (red) and SF2-M4 loop (blue) are indicted. ML335 (black) is shown in sticks with a transparent surface. **b,** Sequence alignment of PD1 for the indicated channels. P1 and M2 helices (blue), SF1 (orange), and SF1-M2 loop (red) are indicated. Terminal residue of the selectivity filter is highlighted. Arrows denote the boundaries of the SF1-M2 loop. **c,** K_{2P}2.1 (TREK-1):ML335 complex

(white) with a view showing the SF2-M4 loop. SF1-M2 loop (red) and SF2-M4 loop (blue) are indicted. ML335 (black) is shown in sticks with a transparent surface. **d,** Sequence alignment of PD2 for the indicated channels. Conserved residues are shaded in slate. Dashed red and blue boxes indicate the SF1-M2 (**c**) and SF2-M4 loops (**d**). Conserved selectivity filter N/D is shaded orange. Pro150, Ala259, and equivalents are shaded red. **e,** Per-frame probability of finding a particular number of hydrogen bonds to the Glu234 sidechain carboxylate in all K_{2P}2.1 (TREK-1) simulations. Dotted lines indicate the overall average number of hydrogen bonds calculated for each simulation condition. **f,** Per-frame probability of a hydrogen bond between the indicated groups in all K_{2P}2.1 (TREK-1) simulations. **g,** Sequence alignment of M1 for the indicated channels. Conserved glutamate is highlighted red.

Sequences (**b**,**d**, and **g**) are from human K_{2P} channels: K_{2P}2.1 (TREK-1) AAD47569.1, K_{2P}10.1 (TREK-2) NP_612190.1, K_{2P}4.1 (TRAAK) AAI10328.1, K_{2P}3.1 (TASK-1) NP_002237.1, K_{2P}9.1 (TASK-3) NP_001269463.1, K_{2P}5.1 (TASK-2) NP_003731.1, K_{2P}1.1(TWIK-1) NP_002236.1, K_{2P}6.1 (TWIK-2) NP_004814.1, K_{2P}16.1 (TALK-1) NP_115491.1, K_{2P}17.1 (TALK-2) AAK28551.1, K_{2P}12.1 (THIK-2) NP_071338.1, K_{2P}13.1 (THIK-1) NP_071337.2, K_{2P}15.1 (TASK-5) EAW75900.1, K_{2P}18.1 (TRESK) NP_862823.1. SF1 and SF2 sequence and numbers for K_{2P}2.1 (TREK-1)$_{cryst}$ (PDB:6CQ6)(*20*) are identical to that of K_{2P}2.1 (TREK-1) AAD47569.1.

Fig. S8 Lolicato *et al.*

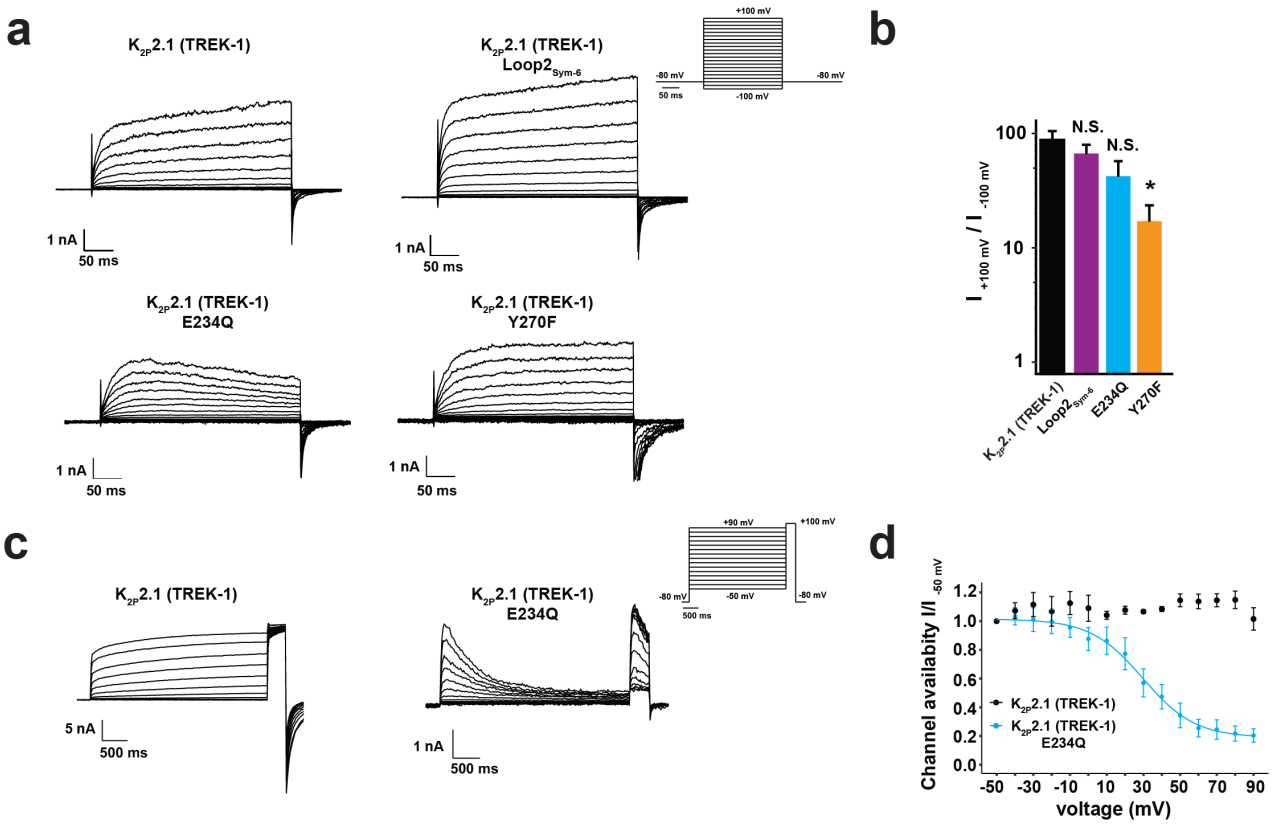

Fig. S8 K_{2P} patch clamp recordings. a, Exemplar current traces from inside-out membrane patches of HEK293 cells expressing $K_{2P}2.1$ (TREK-1), $K_{2P}2.1$ (TREK-1) E234Q, $K_{2P}2.1$ (TREK-1) Y270F, or $K_{2P}2.1$ (TREK1) $Loop2_{Sym6}$, in 150 mM $K^+_{[ext]}$/150 mM $Rb^+_{[int]}$. Inset shows voltage protocol. **b**, Rectification coefficients ($I_{+100mV}/-I_{-100mV}$) calculated from currents recorded on $n \geq 5$ individual patches. * $p < 0.05$ compared to $K_{2P}2.1$ (TREK-1). N.S, not statistically different. **c,** Exemplar current traces from inside-out membrane patches of HEK293 cells expressing $K_{2P}2.1$ (TREK-1) or $K_{2P}2.1$ (TREK-1) E234Q in response to an inactivation protocol (inset). **d,** Channel availability curves determined by plotting the normalized peak currents (I/I_{-50mV}) measured at +100 mV as a function of pre-pulse voltages ($n \geq 4$). For panels **b,** and **d,** data represent mean ± s.e.m.

Fig. S9 Lolicato *et al.*

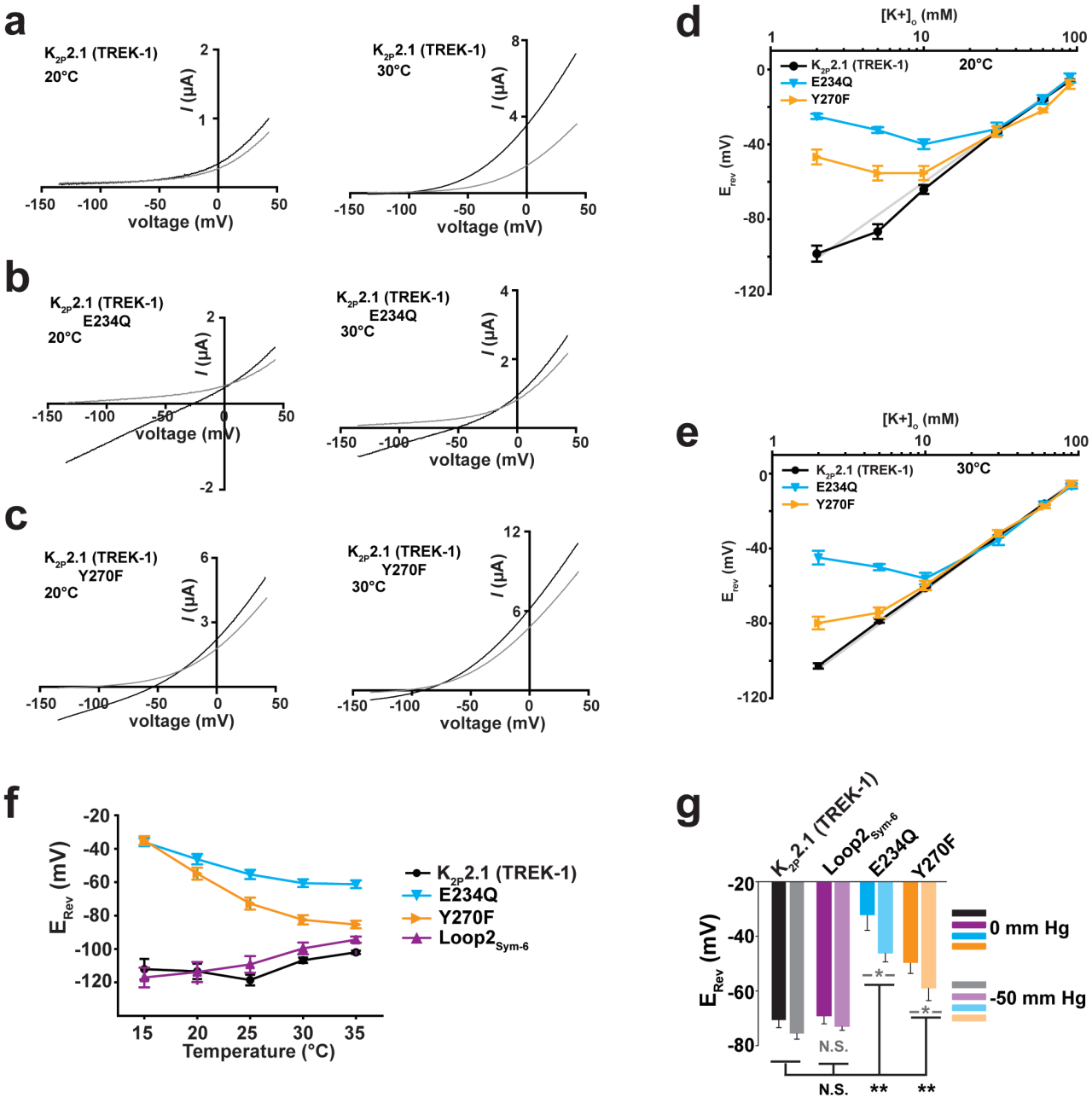

Fig. S9 Activation alters K_{2P}2.1 (TREK-1) mutant ion selectivity. a-c, Exemplar two-electrode voltage clamp (TEVC) recordings of K_{2P}2.1 (TREK-1) (**a**), K_{2P}2.1 (TREK-1) E234Q (**b**), and K_{2P}2.1 (TREK-1) Y270F (**c**) at 20°C (left) and 30°C (right) in solutions of 96 mM Na^+/2 mM K^+ (black) or 96 mM *N*-methyl-D-glucamine/2 mM K^+ (grey). **d,** and **e,** Potassium selectivity recorded in *Xenopus* oocytes in K^+/Na^+ solutions (98.0 mM total) at pH_o = 7.4 at **d**, 20°C and **e**, 30°C (n=6). Data are background subtracted using uninjected oocytes. Grey line represents Nernst equation $E_{rev} = RT/F \times \log([K^+]_o/[K^+]_i)$, where R and F have their usual thermodynamic meanings, z is equal to 1, and T = 20°C or 30°C, assuming $[K^+]_i$ = 108.6 mM ((*110*)). **f,** E_{rev} as a function of temperature for the indicated channels from TEVC experiments in *Xenopus* oocytes. **g,** E_{rev} at 0 and -50 mmHg measured from inside-out membrane patches of HEK293 cells expressing the indicated channels. * $p < 0.05$ compared to K_{2P}2.1 (TREK-1) at the same pressure.

N.S, not statistically different. ($n \geq 4$). Grey indicates statistical significance between the 0 mM and -50 mM Hg measurements. For panels (**d**)-(**g**), data represent mean ± s.e.m.

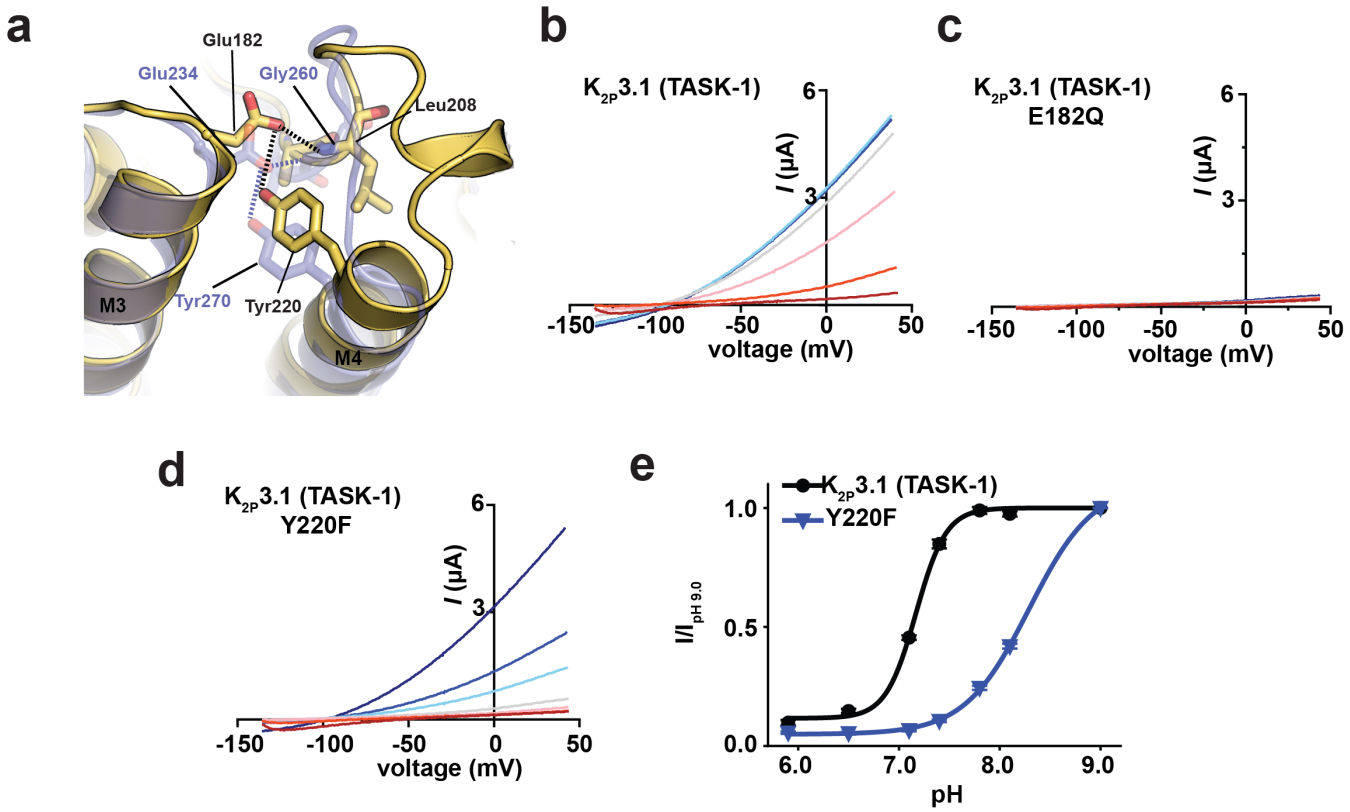

Fig. S10 M3 glutamate network destabilization facilitates K_{2P}3.1(TASK-1) C-type gate closure. **a,** Comparison of the SF2-M4 loop and surrounding elements K_{2P}3.1 (TASK-1) (PDB: 6RV2)(*43*) (yellow) and K_{2P}2.1 (TREK-1) (PBD:6CQ8)(*20*) (transparent purple). Key network residues are shown as sticks and are labeled. Dashed lines show hydrogen bonds. **b-d**, Exemplar two-electrode voltage clamp (TEVC) recordings of **b,** K_{2P}3.1 (TASK-1), **c**, K_{2P}3.1 (TASK-1) E182Q, and **d**, K_{2P}3.1 (TASK1) Y220F at pH_{ext}: 9.0 (dark blue), 8.1 (blue), 7.8 (light blue), 7.4 (grey), 7.1 (pink), 6.5 (red), 5.9 (maroon). **e**, pH activation curves for K_{2P}3.1 (TASK-1) (black) and K_{2P}3.1 (TASK1) Y220F (blue), showing the fraction of the current at 0 mV at each pH relative to the current at pH 9.0 (n≥10). Data in '**e**' represent the mean ± s.e.m. (n≥10).

Supplementary Movie 1 High [K^+]/+40 mV simulation trajectory. Pore helix 1 and SF1-M2 loop are shown in cartoon representation, SF1 is shown as sticks, and potassium ions are spheres of varying colors. Movie represents the first 1920 ns of simulation 1.

Supplementary Movie 2 Low [K^+]/0 mV simulation trajectory. Pore helix 2 and SF2-M4 loop are shown in cartoon representation, SF2 is shown as sticks, M4 is shown as transparent cartoon, and the potassium ion is shown as a magenta sphere. Residues involved in the Glu234 network are shown as green sticks. Movie represents the first 1920 ns of simulation 29.

Supplementary Movie 3 Morph between the SF1 active and inactive conformations. 0 mM [K^+]:ML335 structures and 1 mM [K^+] structures represent the active and inactive conformations, respectively. Selectivity filter is yellow orange. Asn147 and Thr142 are shown as sticks. Potassium ions are magenta spheres.

Supplementary Movie 4 Morph between the SF2 active and inactive conformations. 0 mM [K^+]:ML335 structures and 1 mM [K^+] structures represent the active and inactive conformations, respectively. Selectivity filter is yellow orange. Asp256 and Thr251 are shown as sticks. Potassium ions are magenta spheres.

Table S1 Data collection and refinement statistics $K_{2P}2.1$ (TREK-1) and $K_{2P}2.1$ (TREK-1):ML335 complex structures

Condition	0mM [K+]	1mM [K+]	10mM [K+	30mM [K+]	50mM [K+]	100mM [K+]	200mM [K+]
PDB code	**6W7B**	**6W7C**	**6W7D**	**6W7E**	**6W82**	**6W83**	**6W84**
Data collection							
Space group	$P2_12_12_1$	$P2_12_12_1$	$P2_12_12_1$	$P2_12_12_1$	$P2_12_12_1$	$P2_12_12_1$	$P2_12_12_1$
Cell dimensions							
a, *b*, *c* (Å)	66.91, 122.60, 125.58	66.501, 123.014, 125.848	67.306 122.652 126.127	67.368 122.534 126.552	67.487, 122.067, 126.861	70.222, 121.164, 129.426	70.627, 121.287, 130.034
α, β, γ (°)	90, 90, 90	90, 90, 90	90, 90, 90	90, 90, 90	90, 90, 90	90, 90, 90	90, 90, 90
Resolution (Å)	45.8 - 3.9 (4.0 - 3.9)	44.0 - 3.4 (3.5 - 3.4)	46.0 - 3.5 (3.6 - 3.5)	46.1 - 3.3 (3.4 - 3.3)	46.2 - 3.6 (3.7 - 3.6)	47.6 - 3.9 (4.0 - 3.9)	47.8 - 3.7 (3.8 - 3.7)
$R_{merge,}$	0.196 (7.9)	0.096 (5.14)	0.078 (5.21)	0.051 (5.61)	0.060 (3.01)	0.204 (11.0)	0.141 (9.29)
$I/\sigma(I)$	2.95 (0.34)	9.01 (0.28)	8.20 (0.31)	19.37 (0.44)	8.90 (0.46)	5.80 (0.17)	8.13 (0.22)
$CC_{1/2}$	0.995 (0.264)	0.998 (0.147)	0.998 (0.225)	0.999 (0.326)	0.999 (0.165)	0.997 (0.113)	0.999 (0.120)
Completeness (%)	99.3(99.3)	99.9(100)	99.12 (100)	99.30 (99.9)	99.1 (99.7)	99.9 (99.9)	99.9 (99.6)
Redundancy	4.9 (4.9)	6.5 (6.5)	6.6 (6.7)	11.7 (11.8)	3.6 (3.8)	11.8 (11.3)	13.2 (13.5)
Refinement							
Resolution (Å)	15.0 - 3.9	15.0 – 3.4	15.0 – 3.5	15.0 – 3.3	15.0 – 3.6	15.0 – 3.9	15.0 – 3.7
No. reflections	48795 (4680)	96014 (9500)	90434 (8933)	194227 (19500)	45124 (4759)	123755 (11519)	161238 (15874)
Unique reflections	9972 (955)	14774 (1463)	13692 (1326)	16544 (1647)	12522 (1239)	10520 (1019)	12209 (1174)
R_{work} / R_{free}	0.30/0.36	0.287/0.315	0.276/0.301	0.273/0.317	0.266/0.332	0.264/0.335	0.269/0.339
No. atoms	4168	4234	4263	4204	4295	4366	4353
Protein	4083	4111	4149	4073	4186	4283	4289
Ligand/ion	85	114	123	131	109	83	64
K^+	2	3	2	2	2	6	5
Cd^{++}	2	3	3	3	1	3	3
Lipid	81	108	118	126	106	74	56
ML335	0	0	0	0	0	0	0
B factors							
Protein	235.72	178.88	106.22	154.20	207.38	212.33	167.62
Ligand/ion	183.55	130.71	49.96	158.51	165.76	146.73	67.27
R.m.s. deviations							
Bond lengths (Å)	0.003	0.002	0.004	0.003	0.003	0.003	0.002
Bond angles (°)	0.76	0.62	0.79	0.71	0.65	0.72	0.59
Ramachandran							
Favored (%)	95.1	94.8	94.5	96.22	94.5	95.38	94.67
Allowed (%)	4.9	5.0	5.3	3.78	5.5	4.44	5.15
Outliers (%)	0.0	0.2	0.2	0.0	0.0	0.18	0.18

[a] Values in parentheses are for highest-resolution shell.
Each data set is from a single crystal.

Table S1 Data collection and refinement statistics $K_{2P}2.1$ (TREK-1) and $K_{2P}2.1$ (TREK-1):ML335 complex structures

Condition	ML335:0mM [K+]	ML335:1mM [K+]	ML335:10mM [K+]	ML335:30mM [K+]	ML335:50mM [K+]	ML335:100mM [K+]	ML335:200mM [K+]
PDB code	**6W8F**	**6W8C**	**6W8A**	**6W88**	**6W87**	**6W86**	**6W85**
Data collection							
Space group	$P2_12_12_1$	$P2_12_12_1$	$P2_12_12_1$	$P2_12_12_1$	$P2_12_12_1$	$P2_12_12_1$	$P2_12_12_1$
Cell dimensions							
a, *b*, *c* (Å)	66.671, 119.963, 128.941	67.129, 119.783, 128.872	66.867, 119.951, 129.245	67.006,119.996, 128.794	66.944, 119.48, 128.393	67.317, 120.133, 129.431	70.177, 120.65, 129.795
α, β, γ (°)	90, 90, 90	90, 90, 90	90, 90, 90	90, 90, 90	90, 90, 90	90, 90, 90	90, 90, 90
Resolution (Å)	44.6 - 3.4 (3.5 - 3.4)	46.5 - 2.6 (2.7 - 2.6)	46.5 - 3.0 (3.1 - 3.0)	43.3 - 3.2 (3.3 - 3.2)	44.6 - 3.2 (3.3 - 3.2)	43.5 - 3.3 (3.4 - 3.3)	47.6 - 3.8 (3.9 - 3.8)
$R_{merge,}$	0.117 (4.845)	0.1019 (4.052)	0.1307 (9.36)	0.1337 (4.951)	0.1028 (3.779)	0.1768 (6.905)	0.11 (8.314)
$I/\sigma(I)$	6.04 (0.27)	9.23 (0.40)	6.38 (0.28)	5.38 (0.29)	11.12 (0.53)	5.08 (0.34)	6.66 (0.17)
$CC_{1/2}$	0.995 (0.158)	0.997 (0.192)	0.997 (0.108)	0.996 (0.341)	0.999 (0.199)	0.998 (0.163)	1 (0.113)
Completeness (%)	94.1 (95.0)	98.8 (100)	97.11 (98.8)	95.9 (99.1)	99.81 (99.8)	98.7 (99.4)	99.9 (99.8)
Redundancy	3.9 (3.9)	6.7 (6.9)	5.8 (6.0)	4.7 (5.1)	7.2 (7.0)	6.5 (6.9)	5.9 (6.0)
Refinement							
Resolution (Å)	15.0 – 3.4	15.0 – 2.6	15.0 – 3.0	15.0 – 3.2	15.0 – 3.2	15.0 – 3.3	15.0 – 3.8
No. reflections	54265 (5332)	217375 (22304)	123425 (12506)	81728 (8687)	126742 (11910)	106948 (11156)	65640 (6466)
Unique reflections	13806 (1383)	32673 (3216)	21121 (2069)	17465 (1691)	17607 (1707)	16386 (1623)	11133 (1083)
R_{work} / R_{free}	0.257/0.288	0.243/0.287	0.25/0.271	0.266/0.33	0.24/0.314	0.248/0.295	0.244/0.317
No. atoms	4557	4741	4558	4573	4568	4516	4467
Protein	4349	4341	4349	4358	4343	4349	4350
Ligand/ion	208	399	209	215	225	167	117
K^+	4	6	5	5	5	5	5
Cd^{++}	4	3	4	4	4	3	2
Lipid	154	344	154	160	170	113	64
ML335	46	46	46	46	46	46	46
B factors							
Protein	160.79	118.49	66.39	90.12	141.11	146.49	232.41
Ligand/ion	140.87	134.81	51.59	74.87	125.60	127.03	185.26
R.m.s. deviations							
Bond lengths (Å)	0.002	0.014	0.003	0.006	0.010	0.011	0.011
Bond angles (°)	0.65	1.74	0.70	1.10	1.43	1.49	1.41
Ramachandran							
Favored (%)	95.1	92.71	95.81	93.64	93.07	91.62	93.26
Allowed (%)	4.5	6.38	3.83	6.00	6.02	7.29	5.83
Outliers (%)	0.4	0.91	0.36	0.36	0.91	1.09	0.91

[a] Values in parentheses are for highest-resolution shell.

Each data set is from a single crystal.

Table S2 Anomalous peak heights (in σ)

	1 mM [K^+]	200mM [K^+]	ML335:1mM [K^+]	ML335:200mM [K^+]
Filter site				
S1	2.25	6.24	5.47	6.09
S2	3.10	7.64	6.12	7.01
S3	6.24	8.30	6.40	8.23
S4	3.89	6.19	4.38	4.09
Resolution (Å)	5.5	5.7	5.0	5.5

Anomalous peak heights (in σ) from long-wavelength data above (λ = 3.35 Å) the potassium K-edge as calculated with ANODE(*86*) based on $K_{2P}2.1$ (TREK-1) (6CQ6)(*20*).

Table S3 Molecular dynamics simulations

ID	PDBID	n atoms	Engine	[K^+] (mM)	ML335	Potential (mV)	Length (ns)	n permeations
1	6W8C	205060	Anton2	180	yes	+40	2880	26
2	6W8C	205060	Anton2	180	yes	+40	2880	23
3	6W8C	205060	Anton2	180	yes	+40	2880	9
4	6W8C	205060	Anton2	180	yes	+40	3840	30
5	6W8C	205060	Anton2	180	yes	+40	2880	35
6	6W8C	205228	Anton2	180	yes	+40	3840	26
7	6W8C	205228	Anton2	180	yes	+40	2880	20
8	6W8C	205228	Anton2	180	yes	+40	2880	2
9	6W8C	205228	Anton2	180	yes	+40	2880	29
10	6W8C	205228	Anton2	180	yes	+40	3840	53
11	5VK5	205159	Anton2	180	no	+40	4800	3
12	5VK5	205159	Anton2	180	no	+40	4800	36
13	6CQ6	205175	Anton2	180	no	+40	1920	3
14	6CQ6	205175	Anton2	180	no	+40	1920	2
15	6CQ6	205175	Anton2	180	no	+40	1920	2
16	6CQ6	205175	Anton2	180	no	+40	1920	-1
17	6CQ6	205175	Anton2	180	no	+40	2880	19
18	6CQ6	205325	Anton2	180	no	+40	3840	20
19	6CQ6	205325	Anton2	180	no	+40	2880	18
20	6CQ6	205325	Anton2	180	no	+40	2880	6
21	6CQ6	205325	Anton2	180	no	+40	2880	2
22	6CQ6	205325	Anton2	180	no	+40	3840	34
23	6CQ6	204174	gromacs	5	no	0	1400	-
24	6CQ6	204168	gromacs	5	no	0	2400	-
25	6CQ6	204168	gromacs	5	no	0	2000	-
26	6CQ6	204006	gromacs	5	no	0	2000	-
27	6CQ6	204006	gromacs	5	no	0	2000	-
28	6CQ6	204174	Anton2	5	no	0	3600	-
29	6CQ6	204441	Anton2	5	no	0	3600	-
30	6CQ6	204006	Anton2	5	no	0	3600	-

REFERENCES AND NOTES

1. P. Enyedi, G. Czirjak, Molecular background of leak K^+ currents: Two-pore domain potassium channels. *Physiol. Rev.* **90**, 559–605 (2010).

2. S. Feliciangeli, F. C. Chatelain, D. Bichet, F. Lesage, The family of K2P channels: Salient structural and functional properties. *J. Physiol.* **593** (Pt. 12), 2587–2603 (2015).

3. S. N. Bagriantsev, K. A. Clark, D. L. Minor, Jr., Metabolic and thermal stimuli control K(2P)2.1 (TREK-1) through modular sensory and gating domains. *EMBO J.* **31**, 3297–3308 (2012).

4. S. N. Bagriantsev, R. Peyronnet, K. A. Clark, E. Honore, D. L. Minor Jr., Multiple modalities converge on a common gate to control K2P channel function. *EMBO J.* **30**, 3594–3606 (2011).

5. M. Schewe, E. Nematian-Ardestani, H. Sun, M. Musinszki, S. Cordeiro, G. Bucci, B. L. de Groot, S. J. Tucker, M. Rapedius, T. Baukrowitz, A non-canonical voltage-sensing mechanism controls gating in K2P K^+ channels. *Cell* **164**, 937–949 (2016).

6. P. L. Piechotta, M. Rapedius, P. J. Stansfeld, M. K. Bollepalli, G. Erhlich, I. Andres-Enguix, H. Fritzenschaft, N. Decher, M. S. P. Sansom, S. J. Tucker, T. Baukrowitz, The pore structure and gating mechanism of K2P channels. *EMBO J.* **30**, 3607–3619 (2011).

7. J. Lopez-Barneo, T. Hoshi, S. H. Heinemann, R. W. Aldrich, Effects of external cations and mutations in the pore region on C-type inactivation of Shaker potassium channels. *Receptors Channels* **1**, 61–71 (1993).

8. T. Baukrowitz, G. Yellen, Modulation of K^+ current by frequency and external $[K^+]$: A tale of two inactivation mechanisms. *Neuron* **15**, 951–960 (1995).

9. L. A. Pardo, S. H. Heinemann, H. Terlau, U. Ludewig, C. Lorra, O. Pongs, W. Stuhmer, Extracellular K^+ specifically modulates a rat brain K+ channel. *Proc. Natl. Acad. Sci. U.S.A.* **89**, 2466–2470 (1992).

10. A. Cohen, Y. Ben-Abu, S. Hen, N. Zilberberg, A novel mechanism for human $K_{2P}2.1$ channel gating. Facilitation of C-type gating by protonation of extracellular histidine residues. *J. Biol. Chem.* **283**, 19448–19455 (2008).

11. J. F. Cordero-Morales, L. G. Cuello, Y. Zhao, V. Jogini, D. M. Cortes, B. Roux, E. Perozo, Molecular determinants of gating at the potassium-channel selectivity filter. *Nat. Struct. Mol. Biol.* **13**, 311–318 (2006).

12. T. Hoshi, C. M. Armstrong, C-type inactivation of voltage-gated K^+ channels: Pore constriction or dilation? *J. Gen. Physiol.* **141**, 151–160 (2013).

13. Y. Zhou, R. MacKinnon, The occupancy of ions in the K^+ selectivity filter: Charge balance and coupling of ion binding to a protein conformational change underlie high conduction rates. *J. Mol. Biol.* **333**, 965–975 (2003).

14. Y. Zhou, J. H. Morais-Cabral, A. Kaufman, R. MacKinnon, Chemistry of ion coordination and hydration revealed by a K^+ channel-Fab complex at 2.0 Å resolution. *Nature* **414**, 43–48 (2001).

15. L. G. Cuello, D. M. Cortes, E. Perozo, The gating cycle of a K^+ channel at atomic resolution. *eLife* **6**, e28032 (2017).

16. L. G. Cuello, V. Jogini, D. M. Cortes, E. Perozo, Structural mechanism of C-type inactivation in K^+ channels. *Nature* **466**, 203–208 (2010).

17. V. Pau, Y. Zhou, Y. Ramu, Y. Xu, Z. Lu, Crystal structure of an inactivated mutant mammalian voltage-gated K^+ channel. *Nat. Struct. Mol. Biol.* **24**, 857–865 (2017).

18. W. Wang, R. MacKinnon, Cryo-EM structure of the open human ether-à-go-go-related K^+ Channel hERG. *Cell* **169**, 422–430.e10 (2017).

19. D. Matthies, C. Bae, G. E. S. Toombes, T. Fox, A. Bartesaghi, S. Subramaniam, K. J. Swartz, Single-particle cryo-EM structure of a voltage-activated potassium channel in lipid nanodiscs. *eLife* **7**, e37558 (2018).

20. M. Lolicato, C. Arrigoni, T. Mori, Y. Sekioka, C. Bryant, K. A. Clark, D. L. Minor Jr, $K_{2P}2.1$ (TREK-1)–activator complexes reveal a cryptic selectivity filter binding site. *Nature* **547**, 364–368 (2017).

21. Y. Y. Dong, A. C. W. Pike, A. Mackenzie, C. McClenaghan, P. Aryal, L. Dong, A. Quigley, M. Grieben, S. Goubin, S. Mukhopadhyay, G. F. Ruda, M. V. Clausen, L. Cao, P. E. Brennan, N. A. Burgess-Brown, M. S. P. Sansom, S. J. Tucker, E. P. Carpenter, K2P channel gating mechanisms revealed by structures of TREK-2 and a complex with Prozac. *Science* **347**, 1256–1259 (2015).

22. S. G. Brohawn, J. del Marmol, R. MacKinnon, Crystal structure of the human K2P TRAAK, a lipid- and mechano-sensitive K^+ ion channel. *Science* **335**, 436–441 (2012).

23. S. G. Brohawn, E. B. Campbell, R. MacKinnon, Domain-swapped chain connectivity and gated membrane access in a Fab-mediated crystal of the human TRAAK K^+ channel. *Proc. Natl. Acad. Sci. U.S.A.* **110**, 2129–2134 (2013).

24. S. G. Brohawn, E. B. Campbell, R. MacKinnon, Physical mechanism for gating and mechanosensitivity of the human TRAAK K^+ channel. *Nature* **516**, 126–130 (2014).

25. M. Lolicato, P. M. Riegelhaupt, C. Arrigoni, K. A. Clark, D. L. Minor Jr., Transmembrane helix straightening and buckling underlies activation of mechanosensitive and thermosensitive K(2P) channels. *Neuron* **84**, 1198–1212 (2014).

26. A. N. Miller, S. B. Long, Crystal structure of the human two-pore domain potassium channel K2P1. *Science* **335**, 432–436 (2012).

27. M. G. Derebe, D. B. Sauer, W. Zeng, A. Alam, N. Shi, Y. Jiang, Tuning the ion selectivity of tetrameric cation channels by changing the number of ion binding sites. *Proc. Natl. Acad. Sci. U.S.A.* **108**, 598–602 (2011).

28. D. Liebschner, P. V. Afonine, N. W. Moriarty, B. K. Poon, O. V. Sobolev, T. C. Terwilliger, P. D. Adams, Polder maps: Improving OMIT maps by excluding bulk solvent. *Acta Crystallogr. D Struct. Biol.* **73**, 148–157 (2017).

29. P. S. Langan, V. G. Vandavasi, K. L. Weiss, P. V. Afonine, K. el Omari, R. Duman, A. Wagner, L. Coates, Anomalous x-ray diffraction studies of ion transport in K^+ channels. *Nat. Commun.* **9**, 4540 (2018).

30. A. Wagner, R. Duman, K. Henderson, V. Mykhaylyk, In-vacuum long-wavelength macromolecular crystallography. *Acta Crystallogr. D Struct. Biol.* **72**, 430–439 (2016).

31. J. Ostmeyer, S. Chakrapani, A. C. Pan, E. Perozo, B. Roux, Recovery from slow inactivation in K^+ channels is controlled by water molecules. *Nature* **501**, 121–124 (2013).

32. A. Altis, P. H. Nguyen, R. Hegger, G. Stock, Dihedral angle principal component analysis of molecular dynamics simulations. *J. Chem. Phys.* **126**, 244111 (2007).

33. S. B. Long, X. Tao, E. B. Campbell, R. MacKinnon, Atomic structure of a voltage-dependent K^+ channel in a lipid membrane-like environment. *Nature* **450**, 376–382 (2007).

34. J. T. Brennecke, B. L. de Groot, Mechanism of mechanosensitive gating of the TREK-2 potassium channel. *Biophys. J.* **114**, 1336–1343 (2018).

35. M. P. Harrigan, K. A. McKiernan, V. Shanmugasundaram, R. A. Denny, V. S. Pande, Markov modeling reveals novel intracellular modulation of the human TREK-2 selectivity filter. *Sci. Rep.* **7**, 632 (2017).

36. N. Shi, S. Ye, A. Alam, L. Chen, Y. Jiang, Atomic structure of a Na^+- and K^+-conducting channel. *Nature* **440**, 570–574 (2006).

37. L. Pope, C. Arrigoni, H. Lou, C. Bryant, A. Gallardo-Godoy, A. R. Renslo, D. L. Minor Jr., Protein and chemical determinants of BL-1249 action and selectivity for K_{2P} channels. *ACS Chem. Nerosci.* **9**, 3153–3165 (2018).

38. M. Schewe, H. Sun, Ü. Mert, A. Mackenzie, A. C. W. Pike, F. Schulz, C. Constantin, K. S. Vowinkel, L. J. Conrad, A. K. Kiper, W. Gonzalez, M. Musinszki, M. Tegtmeier, D. C. Pryde, H. Belabed, M. Nazare, B. L. de Groot, N. Decher, B. Fakler, E. P. Carpenter, S. J. Tucker, T.

Baukrowitz, A pharmacological master key mechanism that unlocks the selectivity filter gate in K^+ channels. *Science* **363**, 875–880 (2019).

39. N. Zilberberg, N. Ilan, S. A. N. Goldstein, KCNKØ. *Neuron* **32**, 635–648 (2001).

40. H. P. Larsson, F. Elinder, A conserved glutamate is important for slow inactivation in K^+ channels. *Neuron* **27**, 573–583 (2000).

41. P. Ortega-Sáenz, R. Pardal, A. Castellano, J. López-Barneo, Collapse of conductance is prevented by a glutamate residue conserved in voltage-dependent K^+ channels. *J. Gen. Physiol.* **116**, 181–190 (2000).

42. G. Sandoz, D. Douguet, F. Chatelain, M. Lazdunski, F. Lesage, Extracellular acidification exerts opposite actions on TREK1 and TREK2 potassium channels via a single conserved histidine residue. *Proc. Natl. Acad. Sci. U.S.A.* **106**, 14628–14633 (2009).

43. K. E. J. Rödström, A. K. Kiper, W. Zhang, S. Rinné, A. C. W. Pike, M. Goldstein, L. J. Conrad, M. Delbeck, M. G. Hahn, H. Meier, M. Platzk, A. Quigley, D. Speedman, L. Shrestha, S. M. M. Mukhopadhyay, N. A. Burgess-Brown, S. J. Tucker, T. Müller, N. Decher, E. P. Carpenter, A lower X-gate in TASK channels traps inhibitors within the vestibule. *Nature* **582**, 443–447 (2020).

44. S. A. Pless, J. D. Galpin, A. P. Niciforovic, H. T. Kurata, C. A. Ahern, Hydrogen bonds as molecular timers for slow inactivation in voltage-gated potassium channels. *eLife* **2**, e01289 (2013).

45. J. P. Lees-Miller, Y. Duan, G. Q. Teng, K. Thorstad, H. J. Duff, Novel gain-of-function mechanism in K^+ channel-related long-QT syndrome: Altered gating and selectivity in the HERG1 N629D mutant. *Circ. Res.* **86**, 507–513 (2000).

46. W. E. Miranda, K. R. DeMarco, J. Guo, H. J. Duff, I. Vorobyov, C. E. Clancy, S. Y. Noskov, Selectivity filter modalities and rapid inactivation of the hERG1 channel. *Proc. Natl. Acad. Sci. U.S.A.* **117**, 2795–2804 (2020).

47. D. Bockenhauer, N. Zilberberg, S. A. N. Goldstein, KCNK2: Reversible conversion of a hippocampal potassium leak into a voltage-dependent channel. *Nat. Neurosci.* **4**, 486–491 (2001).

48. M. V. Clausen, V. Jarerattanachat, E. P. Carpenter, M. S. P. Sansom, S. J. Tucker, Asymmetric mechanosensitivity in a eukaryotic ion channel. *Proc. Natl. Acad. Sci. U.S.A.* **114**, E8343–E8351 (2017).

49. M. Lengyel, G. Czirják, P. Enyedi, Formation of functional heterodimers by TREK-1 and TREK-2 two-pore domain potassium channel subunits. *J. Biol. Chem.* **291**, 13649–13661 (2016).

50. J. Levitz, P. Royal, Y. Comoglio, B. Wdziekonski, S. Schaub, D. M. Clemens, E. Y. Isacoff, G. Sandoz, Heterodimerization within the TREK channel subfamily produces a diverse family of highly regulated potassium channels. *Proc. Natl. Acad. Sci. U.S.A.* **113**, 4194–4199 (2016).

51. S. Blin, I. Ben Soussia, E.-J. Kim, F. Brau, D. Kang, F. Lesage, D. Bichet, Mixing and matching TREK/TRAAK subunits generate heterodimeric K_{2P} channels with unique properties. *Proc. Natl. Acad. Sci. U.S.A.* **113**, 4200–4205 (2016).

52. P. Royal, A. Andres-Bilbe, P. Á. Prado, C. Verkest, B. Wdziekonski, S. Schaub, A. Baron, F. Lesage, X. Gasull, J. Levitz, G. Sandoz, Migraine-associated TRESK mutations increase neuronal excitability through alternative translation initiation and inhibition of TREK. *Neuron* **101**, 232–245.e6 (2019).

53. S. Blin, F. C. Chatelain, S. Feliciangeli, D. Kang, F. Lesage, D. Bichet, Tandem pore domain halothane-inhibited K^+ channel subunits THIK1 and THIK2 assemble and form active channels. *J. Biol. Chem.* **289**, 28202–28212 (2014).

54. V. Renigunta, X. Zou, S. Kling, G. Schlichthörl, J. Daut, Breaking the silence: Functional expression of the two-pore-domain potassium channel THIK-2. *Pflugers Arch.* **466**, 1735–1745 (2014).

55. A. P. Berg, E. M. Talley, J. P. Manger, D. A. Bayliss, Motoneurons express heteromeric TWIK-related acid-sensitive K^+ (TASK) channels containing TASK-1 (KCNK3) and TASK-3 (KCNK9) subunits. *J. Neurosci.* **24**, 6693–6702 (2004).

56. A. Mathie, E. L. Veale, K. P. Cunningham, R. G. Holden, P. D. Wright, Two-pore domain potassium channels as drug targets: Anesthesia and beyond. *Annu. Rev. Pharmacol. Toxicol.* 10.1146/annurev-pharmtox-030920-111536 (2020).

57. K. H. Yuill, P. J. Stansfeld, I. Ashmole, M. J. Sutcliffe, P. R. Stanfield, The selectivity, voltage-dependence and acid sensitivity of the tandem pore potassium channel TASK-1: Contributions of the pore domains. *Pflugers Arch.* **455**, 333–348 (2007).

58. S. Liu, P. J. Focke, K. Matulef, X. Bian, P. Moënne-Loccoz, F. I. Valiyaveetil, S. W. Lockless, Ion-binding properties of a K^+ channel selectivity filter in different conformations. *Proc. Natl. Acad. Sci. U.S.A.* **112**, 15096–15100 (2015).

59. J. Li, J. Ostmeyer, E. Boulanger, H. Rui, E. Perozo, B. Roux, Chemical substitutions in the selectivity filter of potassium channels do not rule out constricted-like conformations for C-type inactivation. *Proc. Natl. Acad. Sci. U.S.A.* **114**, 11145–11150 (2017).

60. J. Li, J. Ostmeyer, L. G. Cuello, E. Perozo, B. Roux, Rapid constriction of the selectivity filter underlies C-type inactivation in the KcsA potassium channel. *J. Gen. Physiol.* **150**, 1408–1420 (2018).

61. P. K. Devaraneni, A. G. Komarov, C. A. Costantino, J. J. Devereaux, K. Matulef, F. I. Valiyaveetil, Semisynthetic K^+ channels show that the constricted conformation of the selectivity filter is not the C-type inactivated state. *Proc. Natl. Acad. Sci. U.S.A.* **110**, 15698–15703 (2013).

62. E. A. W. van der Cruijsen, D. Nand, M. Weingarth, A. Prokofyev, S. Hornig, A. A. Cukkemane, A. M. J. J. Bonvin, S. Becker, R. E. Hulse, E. Perozo, O. Pongs, M. Baldus, Importance of lipid-pore loop interface for potassium channel structure and function. *Proc. Natl. Acad. Sci. U.S.A.* **110**, 13008–13013 (2013).

63. L. Ma, D. Roman-Campos, E. D. Austin, M. Eyries, K. S. Sampson, F. Soubrier, M. Germain, D.-A. Trégouët, A. Borczuk, E. B. Rosenzweig, B. Girerd, D. Montani, M. Humbert, J. E. Loyd, R. S. Kass, W. K. Chung, A novel channelopathy in pulmonary arterial hypertension. *N. Engl. J. Med.* **369**, 351–361 (2013).

64. S. Jekhmane, J. Medeiros-Silva, J. Li, F. Kümmerer, C. Müller-Hermes, M. Baldus, B. Roux, M. Weingarth, Shifts in the selectivity filter dynamics cause modal gating in K^+ channels. *Nat. Commun.* **10**, 123 (2019).

65. F. Maingret, I. Lauritzen, A. J. Patel, C. Heurteaux, R. Reyes, F. Lesage, M. Lazdunski, E. Honoré, TREK-1 is a heat-activated background K^+ channel. *EMBO J.* **19**, 2483–2491 (2000).

66. A. J. Patel, E. Honoré, F. Maingret, F. Lesage, M. Fink, F. Duprat, M. Lazdunski, A mammalian two pore domain mechano-gated S-like K^+ channel. *EMBO J.* **17**, 4283–4290 (1998).

67. J. Chemin, A. J. Patel, F. Duprat, I. Lauritzen, M. Lazdunski, E. Honoré, A phospholipid sensor controls mechanogating of the K^+ channel TREK-1. *EMBO J.* **24**, 44–53 (2004).

68. E. Honoré, F. Maingret, M. Lazdunski, A. J. Patel, An intracellular proton sensor commands lipid- and mechano-gating of the K^+ channel TREK-1. *EMBO J.* **21**, 2968–2976 (2002).

69. Y. Kim, H. Bang, C. Gnatenco, D. Kim, Synergistic interaction and the role of C-terminus in the activation of TRAAK K^+ channels by pressure, free fatty acids and alkali. *Pflugers Arch.* **442**, 64–72 (2001).

70. Y. Kim, C. Gnatenco, H. Bang, D. Kim, Localization of TREK-2 K^+ channel domains that regulate channel kinetics and sensitivity to pressure, fatty acids and pH_i. *Pflugers Arch.* **442**, 952–960 (2001).

71. C. McClenaghan, M. Schewe, P. Aryal, E. P. Carpenter, T. Baukrowitz, S. J. Tucker, Polymodal activation of the TREK-2 K2P channel produces structurally distinct open states. *J. Gen. Physiol.* **147**, 497–505 (2016).

72. C. Heurteaux, N. Guy, C. Laigle, N. Blondeau, F. Duprat, M. Mazzuca, L. Lang-Lazdunski, C. Widmann, M. Zanzouri, G. Romey, M. Lazdunski, TREK-1, a K^+ channel involved in neuroprotection and general anesthesia. *EMBO J.* **23**, 2684–2695 (2004).

73. R. M. Lazarenko, M. G. Fortuna, Y. Shi, D. K. Mulkey, A. C. Takakura, T. S. Moreira, P. G. Guyenet, D. A. Bayliss, Anesthetic activation of central respiratory chemoreceptor neurons involves inhibition of a THIK-1-like background K^+ current. *J. Neurosci.* **30**, 9324–9334 (2010).

74. A. Alloui, K. Zimmermann, J. Mamet, F. Duprat, J. Noël, J. Chemin, N. Guy, N. Blondeau, N. Voilley, C. Rubat-Coudert, M. Borsotto, G. Romey, C. Heurteaux, P. Reeh, A. Eschalier, M. Lazdunski, TREK-1, a K^+ channel involved in polymodal pain perception. *EMBO J.* **25**, 2368–2376 (2006).

75. M. Devilliers, J. Busserolles, S. Lolignier, E. Deval, V. Pereira, A. Alloui, M. Christin, B. Mazet, P. Delmas, J. Noel, M. Lazdunski, A. Eschalier, Activation of TREK-1 by morphine results in analgesia without adverse side effects. *Nat. Commun.* **4**, 2941 (2013).

76. D. Vivier, I. B. Soussia, N. Rodrigues, S. Lolignier, M. Devilliers, F. C. Chatelain, L. Prival, E. Chapuy, G. Bourdier, K. Bennis, F. Lesage, A. Eschalier, J. Busserolles, S. Ducki, Development of the first two-pore domain potassium channel TWIK-related K^+ channel 1-selective agonist possessing in vivo antinociceptive activity. *J. Med. Chem.* **60**, 1076–1088 (2017).

77. N. Decher, B. Ortiz-Bonnin, C. Friedrich, M. Schewe, A. K. Kiper, S. Rinné, G. Seemann, R. Peyronnet, S. Zumhagen, D. Bustos, J. Kockskämper, P. Kohl, S. Just, W. González, T. Baukrowitz, B. Stallmeyer, E. Schulze-Bahr, Sodium permeable and "hypersensitive" TREK-1 channels cause ventricular tachycardia. *EMBO Mol. Med.* **9**, 403–414 (2017).

78. X. Wu, Y. Liu, X. Chen, Q. Sun, R. Tang, W. Wang, Z. Yu, M. Xie, Involvement of TREK-1 activity in astrocyte function and neuroprotection under simulated ischemia conditions. *J. Mol. Neurosci.* **49**, 499–506 (2013).

79. W. Kabsch, Xds. *Acta Crystallogr. D Biol. Crystallogr.* **66**, 125–132 (2010).

80. P. R. Evans, G. N. Murshudov, How good are my data and what is the resolution?. *Acta Crystallogr. D Biol. Crystallogr.* **69**, 1204–1214 (2013).

81. P. A. Karplus, K. Diederichs, Assessing and maximizing data quality in macromolecular crystallography. *Curr. Opin. Struct. Biol.* **34**, 60–68 (2015).

82. P. Emsley, K. Cowtan, Coot: Model-building tools for molecular graphics. *Acta Crystallogr. D Biol. Crystallogr.* **60**, 2126–2132 (2004).

83. Collaborative Computational Project, Number 4, The CCP4 suite: Programs for protein crystallography. *Acta Crystallogr. D Biol. Crystallogr.* **50**, 760–763 (1994).

84. P. D. Adams, P. V. Afonine, G. Bunkóczi, V. B. Chen, I. W. Davis, N. Echols, J. J. Headd, L.-W. Hung, G. J. Kapral, R. W. Grosse-Kunstleve, A. J. McCoy, N. W. Moriarty, R. Oeffner, R. J. Read, D. C. Richardson, J. S. Richardson, T. C. Terwilliger, P. H. Zwart, PHENIX: A comprehensive Python-based system for macromolecular structure solution. *Acta Crystallogr. D Biol. Crystallogr.* **66**, 213–221 (2010).

85. O. S. Smart, T. O. Womack, C. Flensburg, P. Keller, W. Paciorek, A. Sharff, C. Vonrhein, G. Bricogne, Exploiting structure similarity in refinement: Automated NCS and target-structure restraints in BUSTER. *Acta Crystallogr. D Biol. Crystallogr.* **68**, 368–380 (2012).

86. A. Thorn, G. M. Sheldrick, ANODE: Anomalous and heavy-atom density calculation. *J. Appl. Cryst.* **44**, 1285–1287 (2011).

87. P. S. Huang, Y.-E. A. Ban, F. Richter, I. Andre, R. Vernon, W. R. Schief, D. Baker, RosettaRemodel: A generalized framework for flexible backbone protein design. *PLOS ONE* **6**, e24109 (2011).

88. S. Jo, T. Kim, W. Im, Automated builder and database of protein/membrane complexes for molecular dynamics simulations. *PLOS ONE* **2**, e880 (2007).

89. J. Huang, S. Rauscher, G. Nawrocki, T. Ran, M. Feig, B. L. de Groot, H. Grubmüller, A. D. MacKerell Jr., CHARMM36m: An improved force field for folded and intrinsically disordered proteins. *Nat. Methods* **14**, 71–73 (2017).

90. J. B. Klauda, R. M. Venable, J. A. Freites, J. W. O'Connor, D. J. Tobias, C. Mondragon-Ramirez, I. Vorobyov, A. D. MacKerell Jr., R. W. Pastor, Update of the CHARMM all-atom additive force field for lipids: Validation on six lipid types. *J. Phys. Chem. B* **114**, 7830–7843 (2010).

91. W. L. Jorgensen, J. Chandrasekhar, J. D. Madura, R. W. Impey, M. L. Klein, Comparison of simple potential functions for simulating liquid water. *J. Chem. Phys.* **79**, 926–935 (1983).

92. K. Vanommeslaeghe, E. Hatcher, C. Acharya, S. Kundu, S. Zhong, J. Shim, E. Darian, O. Guvench, P. Lopes, I. Vorobyov, A. D. Mackerell Jr., CHARMM general force field: A force field for drug-like molecules compatible with the CHARMM all-atom additive biological force fields. *J. Comput. Chem.* **31**, 671–690 (2010).

93. K. Vanommeslaeghe, A. D. MacKerell Jr., Automation of the CHARMM General Force Field (CGenFF) I: Bond perception and atom typing. *J. Chem. Inf. Model.* **52**, 3144–3154 (2012).

94. K. Vanommeslaeghe, E. P. Raman, A. D. MacKerell Jr., Automation of the CHARMM General Force Field (CGenFF) II: Assignment of bonded parameters and partial atomic charges. *J. Chem. Inf. Model.* **52**, 3155–3168 (2012).

95. D. Beglov, B. Roux, Finite representation of an infinite bulk system: Solvent boundary potential for computer simulations. *J. Chem. Phys.* **100**, 9050–9063 (1994).

96. D. E. Shaw, J. P. Grossman, J. A. Bank, B. Batson, J. A. Butts, J. C. Chao, M. M. Deneroff, R. O. Dror, A. Even, C. H. Fenton, A. Forte, J. Gagliardo, G. Gill, B. Greskamp, C. R. Ho, D. J. Ierardi, L. Iserovich, J. S. Kuskin, R. H. Larson, T. Layman, L.-S. Lee, A. K. Lerer, C. Li, D. Killebrew, K. M. Mackenzie, S. Y.-H. Mok, M. A. Moraes, R. Mueller, L. J. Nociolo, J. L. Peticolas, T. Quan, D. Ramot, J. K. Salmon, D. P. Scarpazza, U. B. Schafer, N. Siddique, C. W. Snyder, J. Spengler, P. T.

P. Tang, M. Theobald, H. Toma, B. Towles, B. Vitale, S. C. Wang, C. Young, Anton 2: Raising the bar for performance and programmability in a special-purpose molecular dynamics supercomputer, in *Proceedings of the International Conference for High Performance Computing, Networking, Storage and Analysis* (*SC '14*) (IEEE, 2014), pp. 41–53.

97. M. J. Abraham, T. Murtola, R. Schulz, S. Páll, J. C. Smith, B. Hess, E. Lindahl, GROMACS: High performance molecular simulations through multi-level parallelism from laptops to supercomputers. *SoftwareX* **1-2**, 19–25 (2015).

98. J. Gumbart, F. Khalili-Araghi, M. Sotomayor, B. Roux, Constant electric field simulations of the membrane potential illustrated with simple systems. *Biochim. Biophys. Acta* **1818**, 294–302 (2012).

99. J. C. Phillips, R. Braun, W. Wang, J. Gumbart, E. Tajkhorshid, E. Villa, C. Chipot, R. D. Skeel, L. Kalé, K. Schulten, Scalable molecular dynamics with NAMD. *J. Comput. Chem.* **26**, 1781–1802 (2005).

100. G. J. Martyna, D. J. Tobias, M. L. Klein, Constant-pressure molecular-dynamics algorithms. *J. Chem. Phys.* **101**, 4177–4189 (1994).

101. S. Nosé, A molecular dynamics method for simulations in the canonical ensemble. *Mol. Phys.* **52**, 255–268 (1984).

102. W. G. Hoover, Canonical dynamics: Equilibrium phase-space distributions. *Phys. Rev. A* **31**, 1695–1697 (1985).

103. Y. Shan, J. L. Klepeis, M. P. Eastwood, R. O. Dror, D. E. Shaw, Gaussian split Ewald: A fast Ewald mesh method for molecular simulation. *J. Chem. Phys.* **122**, 054101 (2005).

104. J.-P. Ryckaert, G. Ciccotti, H. J. C. Berendsen, Numerical integration of the cartesian equations of motion of a system with constraints: Molecular dynamics of *n*-alkanes. *J. Comput. Phys.* **23**, 327–341 (1977).

105. M. Parrinello, A. Rahman, Polymorphic transitions in single-crystals: A new molecular-dynamics method. *J. Appl. Phys.* **52**, 7182–7190 (1981).

106. S. Nosé, M. L. Klein, Constant pressure molecular-dynamics for molecular systems. *Mol. Phys.* **50**, 1055–1076 (2006).

107. T. Darden, D. York, L. Pedersen, Particle mesh Ewald: An N·log(N) method for Ewald sums in large systems. *J. Chem. Phys.* **98**, 10089–10092 (1993).

108. B. Hess, H. Bekker, H. J. C. Berendsen, J. G. E. M. Fraaije, LINCS: A linear constraint solver for molecular simulations. *J. Comput. Chem.* **18**, 1463–1472 (1997).

109. N. Michaud-Agrawal, E. J. Denning, T. B. Woolf, O. Beckstein, MDAnalysis: A toolkit for the analysis of molecular dynamics simulations. *J. Comput. Chem.* **32**, 2319–2327 (2011).

110. H. Guizouarn, N. Gabillat, R. Motais, F. Borgese, Multiple transport functions of a red blood cell anion exchanger, tAE1: Its role in cell volume regulation. *J. Physiol.* **535**, 497–506 (2001).